Materials Science & Engineering A 939 (2025) 148446

Contents lists available at ScienceDirect

Materials Science & Engineering A

journal homepage: www.elsevier.com/locate/msea

Additive manufacturing of strong and ductile In939+TiB_2 by laser powder bed fusion

Jong-Soo Bae [a,1], Emre Tekoglu [b,1], Mohammed Alrizqi [c], Alexander D. O'Brien [a], Jian Liu [d], Krista Biggs [e], So Yeon Kim [a,e], Aubrey Penn [f], Ivo Sulak [g], Wen Chen [d], Kang Pyo So [a], A. John Hart [h], Gi-Dong Sim [a,*], Ju Li [b,e,**]

[a] Department of Mechanical Engineering, Korea Advanced Institute of Science and Technology, 291 Daehak-ro, Yuseong-gu, Daejeon, 34141, Republic of Korea
[b] Department of Nuclear Science and Engineering, Massachusetts Institute of Technology, Cambridge, MA, 02139, USA
[c] Sibley School of Mechanical and Aerospace Engineering, Cornell University, Ithaca, NY, 14853, USA
[d] Department of Mechanical and Industrial Engineering, University of Massachusetts, Amherst, MA, 01003, USA
[e] Department of Materials Science and Engineering, Massachusetts Institute of Technology, Cambridge, MA, 02139, USA
[f] MIT.nano, Massachusetts Institute of Technology, Cambridge, MA, 02139, USA
[g] Institute of Physics of Materials, Czech Academy of Sciences, Žižkova 22, 616 00, Brno, Czech Republic
[h] Department of Mechanical Engineering, Massachusetts Institute of Technology, Cambridge, MA, 02139, USA

ARTICLE INFO

Keywords:
Laser powder bed fusion
Ni-based superalloy
Additive manufacturing
Mechanical property
In-situ alloying

ABSTRACT

Improving the printability and high-temperature mechanical performance of high aluminum and titanium content Inconel superalloys is of interest in aerospace, automotive, and energy industries. In aerospace applications, for instance, components such as turbine blades and engine parts require exceptional strength and ductility under extreme temperatures (above 800 °C), which more common Inconel alloys such as In718 and In625 struggle to provide. Therefore, this study explores the influence of TiB_2 on the additive manufacturing of Inconel 939 superalloy (In939) by laser powder bed fusion (LPBF). TiB_2 powders with a size of approximately 1–3 μm were decorated on the surfaces of Inconel 939 alloy powders via high-speed blending. Both pure In939 and In939+TiB_2 samples were prepared by LPBF with varying laser power and scanning speed. Microstructural analysis of the as-printed specimens revealed that the TiB_2 addition to Inconel 939 eliminated crack formation under all LPBF conditions tested. Consequently, the as-printed In939+TiB_2 exhibited superior room temperature (RT) yield strength (1256 MPa) and ultimate tensile strength (1578 MPa) with reasonable tensile ductility (13–15 %) compared to the as-printed In939. Furthermore, In939+TiB_2 shows exceptional high-temperature strength, demonstrating superior performance up to 850°C in contrast to other additively manufactured and cast In939 materials in the literature. This study paves the way for sectors including aerospace, automotive, and energy to significantly enhance the performance of critical components like turbine blades and engine parts made of In939 through LPBF.

1. Introduction

Nickel-based (Ni-based) superalloys, known for their high-temperature strength and corrosion resistance, are widely used in extreme-condition applications. Among the various alloys studied, Inconel 939 (In939) has recently gained particular interest in the additive manufacturing (AM) research community for its unique capability to retain superior mechanical stability at elevated temperatures up to 800–850°C, which is higher than the typical operational limit of other widely used superalloys like Inconel 625 and Inconel 718 [1–5]. However, Inconel 939 faces challenges in printability due to solidification cracking, especially in AM processes such as laser powder bed fusion (LPBF). These cracks, resulting from high residual stresses and phase segregation, hinder its effective use without post-processing or modification strategies [1–11]. Recent studies have demonstrated that crack-free In939 can be produced via LPBF under strictly controlled

* Corresponding author.
** Corresponding author. Department of Nuclear Science and Engineering, Massachusetts Institute of Technology, Cambridge, MA 02139, USA.
E-mail addresses: gdsim@kaist.ac.kr (G.-D. Sim), liju@mit.edu (J. Li).
[1] These authors contributed equally.

https://doi.org/10.1016/j.msea.2025.148446
Received 20 January 2025; Received in revised form 18 April 2025; Accepted 1 May 2025
Available online 14 May 2025

process parameters or through modifications, such as the addition of Si [4]. In contrast, this study introduces an approach to address these challenges by incorporating TiB_2 particles into In939. In this way, we aim to address two key concepts associated with the LPBF of In939 by combining an enlarged printing process window with superior mechanical properties.

Currently, the AM research community is also focusing on developing novel metal matrix composites (MMCs), utilizing ceramic particle reinforcing agents to improve the mechanical and other crucial properties of the base metals, aiming for durability in even more extreme operational conditions [12–17]. A significant area of focus within these developments is MMCs reinforced with TiB_2 ceramics. Transition metal diborides, belonging to the category of ultra-high-temperature ceramics (UHTCs), are strong candidates for fabricating Ni-based MMCs [18,19]. There have been multiple reports on TiB_2-reinforced Ni-based MMCs produced using various AM techniques [13,14,20], including a series of studies by Zhang et al. [21–23]. In this context, the introduction of TiB_2 in In939 is explored here as a strategy to mitigate cracking and enhance the alloy's high-temperature performance, making it more suitable for demanding aerospace applications where components are subjected to extreme thermal and mechanical stresses.

The literature suggests that transition metal diborides have substantial potential to enhance the mechanical performance of both solid-solution and precipitation-strengthened Ni-based superalloys. Zhang et al. [22,24] showed that incorporating TiB_2 into solid-solution strengthened Ni-based superalloys (e.g., GH3230) leads to effective bonding between TiB_2 and the matrix interface, as well as a higher fraction of high-angle grain boundaries. This combination increases strength and facilitates easier slip in the plastic zone compared to pure GH3230. In a similar vein, Tekoglu et al. [25] reported strength improvements of precipitation-strengthened In625 reinforced with TiB_2 at both room temperature (RT) and 800 °C. In the mentioned research, TiB_2 was found to decompose during LPBF, which promoted the formation of Cr-, Mo-, and Nb-rich complex borides due to the locally increased concentration of these elements, contributing to the superior high-temperature strength of In625 [25].

In parallel, several studies have focused on revealing the crack initiation mechanisms and reducing the occurrence of cracks in hard-to-print Ni-based superalloys [23,26–32]. Current strategies for suppressing cracks in these challenging-to-print Ni-based superalloys include (1) micro-alloying [4,31,32], (2) optimization of the LPBF process [30], and (3) the incorporation of heterogeneous nucleating agents such as TiB_2 [23]. The second approach primarily aims to facilitate a transition from columnar to equiaxed grains by varying LPBF conditions, such as altering the laser power, scanning speed, and hatch spacing. However, the first and third methods have been more effective in reducing cracking, as studies have shown crack inhibition by narrowing the solidification temperature range (STR) and promoting grain boundary precipitation of secondary additions during the LPBF process. For In939, Zhang et al. [4] discovered that adding 1.5 and 3.0 wt% Si to In939 significantly reduced crack density in LPBF-processed In939 components, an outcome attributed to a lower cooling rate during LPBF. Additionally, the addition of Si increased the number of precipitates, resulting in higher strength but lower tensile ductility [4]. On the other hand, TiB_2 has proven remarkable effectiveness in mitigating cracking and reducing porosity in Ni-based superalloys [22,23,25]. In one such study, Zhang et al. [23] showed that adding 1 and 2 wt% TiB_2 inhibited solidification and solid-state cracking in LPBF-processed GH3230. The inhibition of cracking mechanisms was attributed to the formation of finer grains, the presence of isolated liquid droplets during solidification, and increased the topological complexity of the grain boundaries.

To date, the impact of TiB_2 or other ceramic reinforcements on the microstructure, crack initiation, and consequent enhancements in tensile properties of LPBF-processed Inconel 939 has not been investigated. Contrary to other studies on TiB_2-reinforced MMCs where TiB_2 particles remain undecomposed [33–35], our study reveals that TiB_2 particles fully decompose, forming new intermetallic compounds that enhance mechanical properties at both room and elevated temperatures. Additionally, the incorporation of TiB_2 demonstrates a remarkable capability to suppress crack formation in the as-printed state. It is important to note that additively manufactured materials exhibiting superior properties in their as-printed state provide significant economic benefits through cost and time savings derived from the streamlined manufacturing process. In this context, our findings underscore the economic viability of employing TiB_2-reinforced In939 components fabricated by LPBF. The following sections will delve into the microstructural features contributing to crack inhibition in TiB_2-reinforced In939 and examine the room and high-temperature mechanical properties of these components fabricated using LPBF.

2. Methods

2.1. Feedstock preparation and LPBF process

The In939+TiB_2 feedstock was prepared by blending In939 powders with 2 vol% TiB_2 particles. The TiB_2 powders, with a particle size of approximately 1–3 μm, were purchased from US Research Nanomaterials Inc., as shown in the scanning electron microscope (SEM) image in Supplementary Fig. 1(a). Supplementary Fig. 1(b) displays the SEM image of commercially available In939 powders with a particle size range of 15–45 μm (D10: 19.7 μm, D50: 29.9 μm, D90: 45.3 μm) and were procured from MATEXCEL. The ceramic powders were added to the In939 powders to form a mixture containing 2 vol% TiB_2. The blending was performed in batches of 500 g in a high-speed blender (VM0104, Vita-Mix, USA) for 90 min, encompassing 9 cycles where each cycle consisted of 10 min of blending followed by 10 min of cooling. Low and high-magnification SEM images and corresponding EDX mappings of the blended In939 + 2 vol% TiB_2 (hereafter referred to as In939+TiB_2) powders are provided in Fig. 1(a and b). The In939 powders mostly retained their sphericity after blending with TiB_2. Energy dispersive X-ray (EDX) mappings of the blended In939+TiB_2 particles reveal that the TiB_2 particles (indicated by yellow arrows) were effectively distributed on the surfaces of the In939 particles. The chemical compositions of the commercial In939 and blended powders were measured via SEM/EDX and are provided in Table 1.

After preparing the In939+2TiB_2 powders, a commercial LPBF system (EOS M290) was utilized to perform AM on both the as-purchased, unreinforced In939 powders and the In939+2TiB_2 powders. Fig. 1(c) illustrates the printed In939 and In939+TiB_2 samples before their removal from AISI 4140 steel build plates. In this study, two types of sample geometries were fabricated. One was in cubic form with dimensions of 2 mm × 2 mm × 2 mm, used for microstructural characterizations. The other was in plate form, measuring 20 mm × 20 mm × 2 mm, from which tensile specimens were cut out using wire electrical discharge machining (EDM). Additionally, the dimensions of the dog-bone specimens prepared for room temperature (RT) and high-temperature (HT) tensile testing are presented in Fig. 1(d) and (e), respectively. Fig. 1(f) shows a representative image of the In939+TiB_2 samples fabricated via LPBF. Lastly, Table 2 shows volumetric energy densities (VEDs) applied to the In939 and the 2 vol% TiB_2 reinforced In939 composite samples.

2.2. Microstructure analysis

After LPBF, the samples were prepared for microstructural characterization through cutting, grinding, and polishing. The relative densities of the LPBF-processed samples were measured using Archimedes' method. The distribution of microcracks and porosity in selected samples was analyzed using computed tomography (CT) with a Zeiss Xradia 620 Versa X-ray microscope. Computed Tomography (CT) was performed to measure the porosity distribution and pore size in the printed samples, using a Zeiss Xradia 620 Versa X-ray microscope. Scanning

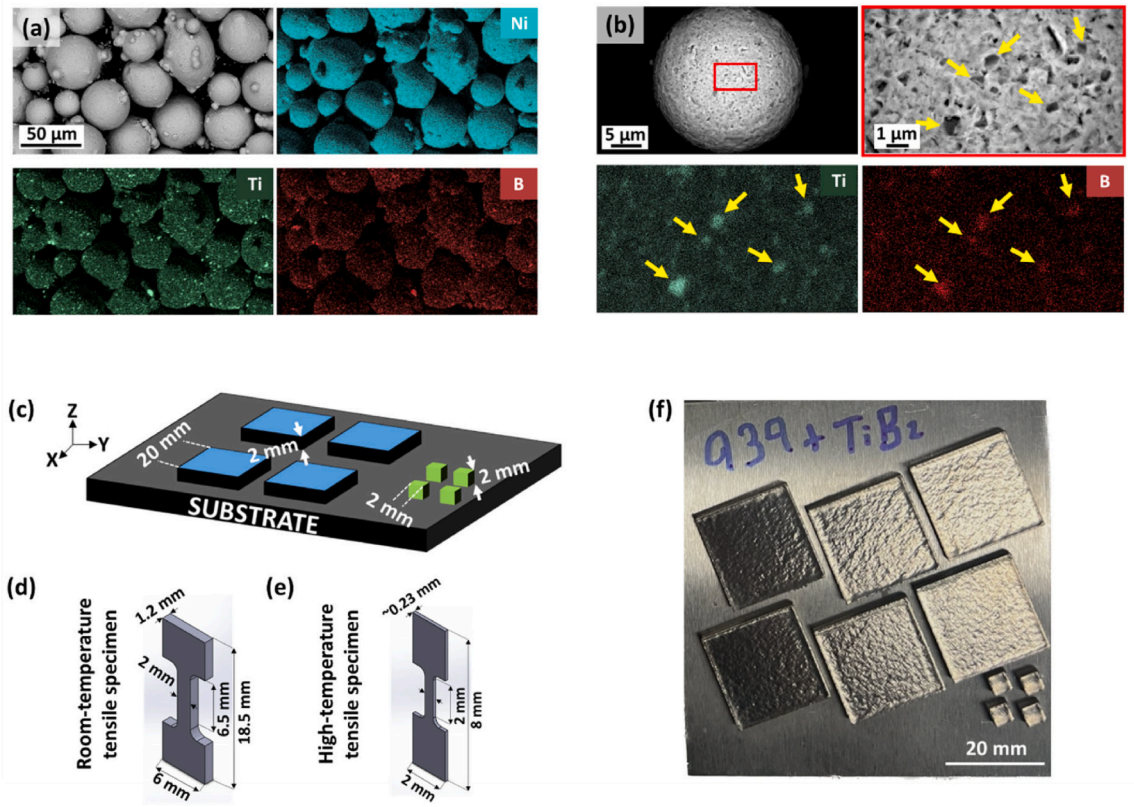

Fig. 1. (a, b) SEM micrographs and EDX mapping analysis of In939 particles decorated with TiB_2 after blending. (c) Illustration of samples produced via LPBF. Geometry and dimensions of (d) room-temperature tensile specimens and (e) high-temperature tensile specimens machined by wire EDM. (f) In939+TiB_2 samples fabricated by LPBF using the EOS M290 system, shown before removal from the build plates.

parameters included a pixel size of 1.75 μm, HE18 filter, 160 keV beam energy, 25 W power, 5 s exposure time, and a full 360° rotation for 4X scans of the 3D printed specimen. Post-processing was conducted using Dragonfly software, where pores smaller than 9 voxels (equivalent to less than 2 μm) were excluded. The phase composition of the powders and LPBF-processed samples was characterized by X-ray diffraction, using a PANalytical Empyrean diffractometer with Cu K_α radiation (λ = 1.54 Å) over a range of scattering angles $2\theta = 10–90°$ and a step size of 0.01°. To determine the microstructural characteristics and chemical composition, a Zeiss Merlin high-resolution scanning electron microscope (SEM) (Carl Zeiss AG, Oberkochen, Germany) was employed. Electron backscatter diffraction (EBSD) analyses were also performed with a step size of 0.5 μm to ensure sufficient resolution for capturing the microstructural features such as cracks. For transmission electron microscopy (TEM) sample preparation, a Raith VELION Focused Ion Beam (FIB) was used. Following FIB preparation, scanning transmission electron microscopy (STEM) imaging, diffraction, and spectroscopy were conducted in a probe-corrected Thermo Fisher Themis Z G3 operated at 200 kV and using a 19 mrad convergence angle. Energy dispersive X-ray spectroscopy (EDX) was collected using a beam current of 200 pA with Super-X detectors. Electron energy-loss spectroscopy (EELS) was also performed in a probe-corrected Thermo Fisher Themis Z G3 equipped with a Gatan Continuum EELS spectrometer. The CALPHAD (CALculation of PHAse Diagrams) method, using the Thermo-Calc software with TTNI8 database, was applied to interpret the hot cracking susceptibility of the LPBF-processed compositions. In this context, Scheil-Gulliver curves were plotted based on the Aziz model [36] for solute trapping, which accounts for the high solidification rates characteristic of additive manufacturing.

2.3. Mechanical testing

Tensile tests were conducted at room temperature using an Instron 5969 with a strain rate of 2×10^{-4} s^{-1}. Three samples from each category were tested to validate the obtained results. The tensile displacement and strain were precisely recorded using a non-contact AVE2 video extensometer. High-temperature tensile tests were performed at 800 and 850°C with a strain rate of 2×10^{-4} s^{-1} using a custom-built mechanical testing machine equipped with a furnace capable of operating up to 1000 °C. Accurate measurement of the gauge section strain was achieved using the digital image correlation (DIC) technique. To ensure stable DIC strain measurement at elevated temperatures, white aluminum oxide aerosol paint, and black heat-resistant paint were sprayed onto the gauge section of each specimen to create high-contrast speckle patterns. Sample images were captured every 2 s during the test using a CCD camera (Teledyne FLIR, Inc.) equipped with a telecentric lens (Edmund Optics, Inc.).

3. Results

3.1. Thermodynamic calculations to evaluate the effect of TiB_2 content

Before LPBF, Scheil-Gulliver simulations were performed to assess the effect of TiB_2 content on the cracking sensitivity coefficient (CSC) and of In939 alloys and determine the feasible composite formulation. Fig. 2(a) shows the Scheil-Gulliver curves with respect to different TiB_2 contents (0, 1, 2 and 5 vol%). Accordingly, the Scheil freezing temperature range and CSC of different compositions are plotted in Fig. 2(b). The criterion of Clyne and Davies [37] is used to calculate CSC:

$$CSC = \frac{t_V}{t_R}. \quad (1)$$

Table 1
EDX results obtained from raw In939 powders (Supplementary Fig. 1(b)) and In939 + 2TiB_2 powders after blending (Fig. 1 (b)).

Element (wt%)	Ni	Cr	Co	W	Nb	Ti	Al	Ta	Zr	C	B
Commercial In939	48.14 ± 0.33	22.51 ± 0.42	19.34 ± 0.60	1.96 ± 0.11	0.94 ± 0.13	3.71 ± 0.27	1.80 ± 0.11	1.21 ± 0.07	0.12 ± 0.04	0.27 ± 0.07	–
In939 + TiB_2	47.81 ± 0.27	22.02 ± 0.36	18.51 ± 0.23	1.49 ± 0.15	0.85 ± 0.17	5.3 ± 0.33	1.62 ± 0.15	1.33 ± 0.10	0.04 ± 0.06	0.14 ± 0.09	0.89 ± 0.13

where t_V is the solidifying time period of the alloy when it is vulnerable to hot cracking, and t_R is the time available for stress relief processes.

Katgerman [38] proposed a criterion as follows:

$$CSC = \frac{t_{0.99} - t_{cr}}{t_{cr} - t_{coh}}. \quad (2)$$

t_{cr} and t_{coh}, where t_{cr} is the time when feeding becomes inadequate, and t_{coh} is the time when the fraction solid is at the coherency point.

In this study, the duration of interdendritic separation was assumed as the time required for the solid fraction to increase from 0.9 to 0.99 ($t_{0.99}$-$t_{0.9}$). Similarly, the duration of mass and liquid feeding was defined as the time interval during which the solid fraction increases from 0.4 to 0.9 ($t_{0.9}$-$t_{0.4}$). Therefore, the formulation becomes as follows:

$$CSC = \frac{t_{0.99} - t_{0.9}}{t_{0.9} - t_{0.4}}. \quad (3)$$

It is worth noting that the assumption of linear cooling allows replacing the time measurements with temperature measurements corresponding to the same fraction of solid, read directly from Scheil curves [38]:

$$CSC = \frac{T_{0.9} - T_{0.99}}{T_{0.4} - T_{0.9}}. \quad (4)$$

It is evident that TiB_2 addition into In939 alloy substantially decreases the CSC values (~3 times). It is important to mention that the melting point of In939+5TiB_2 is almost 1700°C, which is 350-450°C higher than the other compositions (i.e., In939, In939+1TiB_2 and In939+2TiB_2). Therefore, the Scheil freezing temperature range of the In939+5TiB_2 is also higher than that of other compositions. Based on these calculations, In939+1TiB_2 and In939+2TiB_2 were selected as the optimal composite formulation for LPBF studies since higher TiB_2 additions are prone to other LPBF-related defects, such as lack of fusion and delamination due to its higher melting temperature. Although the CSC value of In939+1TiB_2 is the lowest, the difference compared to In939+2TiB_2 is minimal, indicating no significant variation in terms of CSC. However, the addition of 2 vol% TiB_2 is expected to have a greater strengthening effect due to its microstructural characteristics than the addition of 1 vol% TiB_2. This strengthening effect of Ti and B has been suggested in other studies for similar alloy systems, where the presence of these elements in solution has been associated with improvements in mechanical properties [39]. Therefore, from this perspective, In939+2TiB_2 was chosen as the optimal composition for this study.

In parallel, Kou [40] proposed a criterion that links the solidification cracking susceptibility (SCI) of an alloy to the slope of the temperature versus square root of solid fraction (T - $f_s^{1/2}$) curve:

$$SCI = \left| dT \Big/ \mathrm{d}\left(f_s^{\frac{1}{2}}\right) \right| near \left(f_s^{\frac{1}{2}}\right). \quad (5)$$

This criterion captures the thermal behavior near the end of solidification by quantifying the steepness of the T - $f_s^{1/2}$ curve. A steeper slope near $f_s^{1/2} = 1$ indicates a narrower mushy zone, corresponding to a higher SCI and, consequently, a greater susceptibility to solidification cracking. Higher SCI values imply a prolonged presence of liquid films along the grain boundaries, which hinder adequate liquid feeding and increase the risk of cracking. Mechanically, this facilitates the opening of grain boundary channels under tensile stress, promoting crack propagation. To compare SCI values across different compositions, Scheil solidification data were processed using Python 3.10. The square root of the solid fraction was computed, and the steepest temperature gradient with respect to $f_s^{1/2}$ near solidification completion ($f_s^{1/2} = 1$) was identified. This maximum value of $|dT/d((f_s)^{1/2})|$ was used to define the SCI.

Fig. 3(a) shows the T - $f_s^{1/2}$ curves for In939 with varying TiB_2 content. Among the four compositions, In939 exhibits the steepest T - $f_s^{1/2}$ slope, indicating a higher susceptibility to solidification cracking. In other words, the narrower mushy zone during the final stage of

Table 2
Volumetric energy densities (VEDs) applied during LPBF process.

Parameter set	P1	P2	P3	P4	P5	P6	P7	P8
Volumetric energy density (J/mm^3)	148.8	104.2	80.1	65.1	178.6	125.0	96.2	78.1

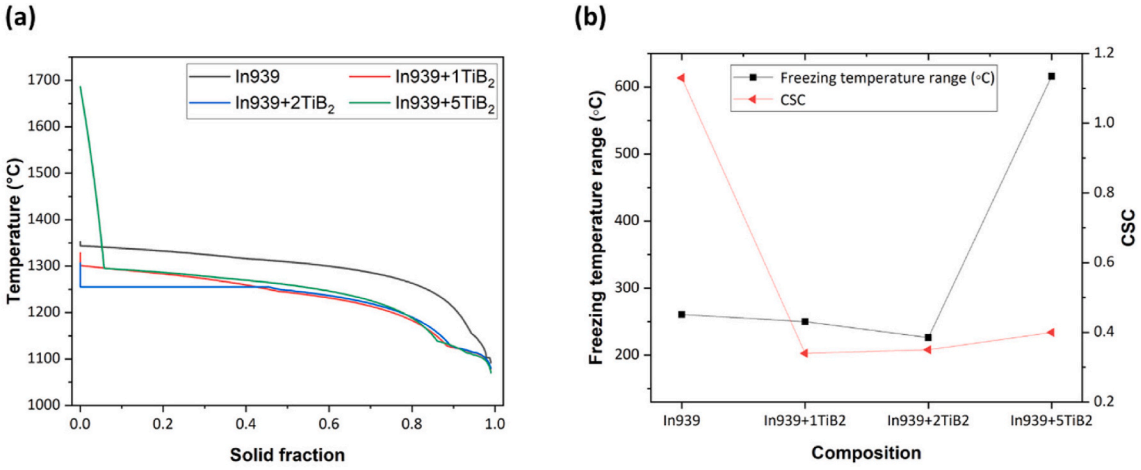

Fig. 2. (a) Scheil-Gulliver curves of In939 with different TiB_2 contents, and (b) Scheil freezing temperature range and CSC values with respect to composite formulations.

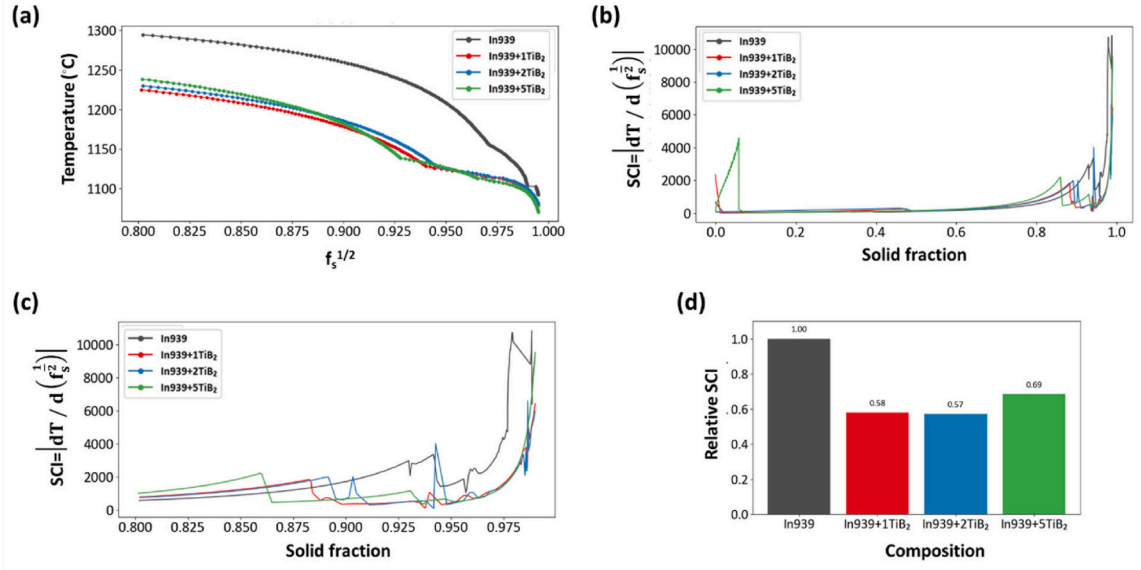

Fig. 3. (a) Temperature vs $f_s^{1/2}$ for In939 and TiB_2-modified composites, showing the evolution of solidification path, (b) SCI calculated as the absolute derivative $|dT/d(f_s)|$ across the full solid fraction range ($0 < f_s < 0.99$), (c) zoomed-in view of SCI vs. solid fraction in the terminal solidification range ($0.8 < f_s < 0.99$), highlighting sensitivity differences between compositions, and (d) relative SCI values ($0 < f_s < 0.99$) normalized to base In939, illustrating reduced cracking susceptibility with 1–2 vol% TiB_2 additions.

solidification renders In939 more prone to cracking compared to the TiB_2-reinforced variants. To quantitatively assess the solidification cracking resistance, SCI values were calculated over the entire solidification range ($0< f_s < 0.99$) as well as a narrower interval $0.8< f_s < 0.99$. Fig. 3(b) presents the SCI - f_s curve over the full solidification range ($0< f_s < 0.99$), revealing that SCI increases with f_s, particularly with a notably sharper rate during the late stage of solidification. This trend is highlighted in Fig. 3(c), which focuses on the interval $0.8<f_s < 0.99$. The calculated SCI values across $0 < f_s < 0.99$ for each composition are as follows: i) In939: 3883.81°C, ii) In939+1TiB_2: 2251.90°C, iii) In939+2TiB_2: 2219.19°C, iv) In939+5TiB_2: 2661.20 °C. For comparative purposes, all calculated SCI values within the range of $0 < f_s < 0.99$ were normalized relative to that of base In939 (Fig. 3(d)).

Based on both criteria employed in this study, In939 was consistently identified as the most crack-susceptible composition, while In939+2TiB_2 emerged as a balanced choice combining low susceptibility and mechanical strengthening benefits. While SCI provides a useful quantitative metric for evaluating solidification cracking susceptibility, it does not fully account for the influence of microstructural features. In particular, the addition of TiB_2 is known to promote grain refinement, which can enhance crack resistance by increasing grain boundary cohesion, improving interdendritic liquid feeding, and

disrupting the continuity of hot tear-prone liquid films. Therefore, even when SCI values are non-zero, the refinement-induced microstructural benefits may still play a critical role in mitigating crack initiation and propagation. To account for these effects, microstructural analyses were conducted, as detailed in later sections, to provide complementary insights beyond thermal susceptibility metrics.

3.2. Defect characterization under various printing conditions

To examine the defects in the as-printed samples fabricated under various LPBF conditions, SEM images were taken from the cross-sections of LPBF-processed In939 and In939+TiB_2 (Fig. 4(a and b)). It is important to note that cracks and porosities are indicated by red and yellow arrows, respectively in Fig. 4. For In939, the optimized parameter set was identified as P4 (VED: 65.1 J/mm^3) (hereafter known as In939), based on measured relative densities under different LPBF parameters (Fig. 4(c)). Regardless of the LPBF parameters, cracking emerged as the prevailing defect formation mechanism in all In939 samples, although some porosities with a maximum diameter of 5–10 μm were also observed. Cross-sectional micrographs and relative densities from pure In939 samples revealed that the density of cracks decreased under optimal LPBF conditions (i.e., P4). However, even under these conditions, cracking of the In939 alloy was still evident. Our results are consistent with the study by Li et al. [11], where LPBF-fabricated In939 samples exhibited cracks across a wide range of printing parameters. They reported that the cracking density was below 0.34 % only under specific printing conditions, while all other parameters resulted in a crack density exceeding 0.7 %. High-magnification SEM images in Supplementary Fig. 2 show that the cracks possess dendritic morphology regardless of their lengths. The length of solid-state cracks generally ranges from 100 to 300 μm—and in some cases, even longer—according to the literature [29]. However, cracks longer than this should not always be considered solid-state cracks; they might also result from the propagation of cracks that initially formed as hot tears [29]. Therefore, regardless of the crack length, it is believed that the cracking mechanism in pure In939 was solidification cracking during this study. Crack formation behavior was examined for all samples produced under varying LPBF conditions. The addition of TiB_2 to the In939 alloy led to a notable reduction in crack density across all process parameters, indicating improved resistance to cracking. In contrast,

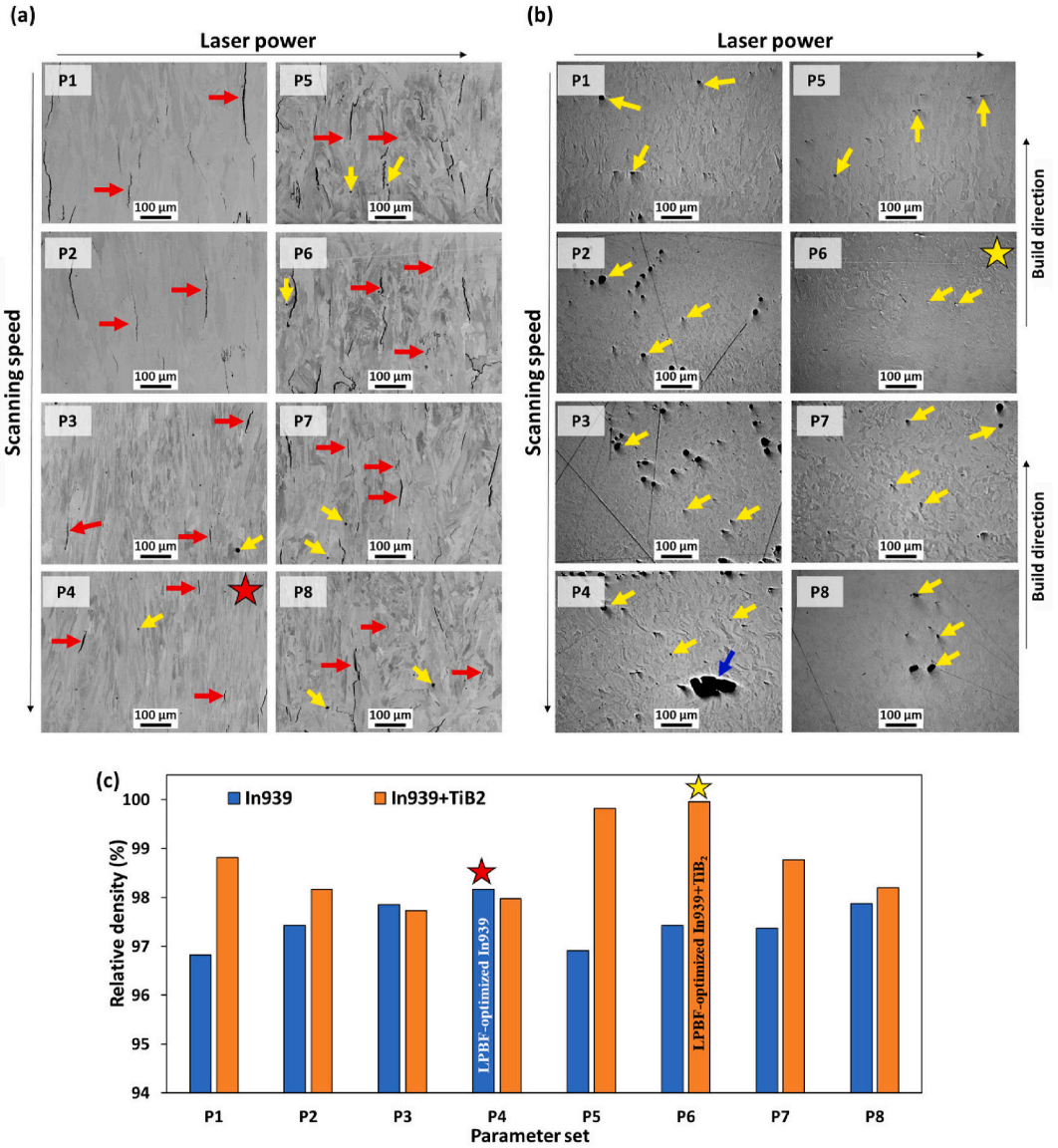

Fig. 4. SEM images of LPBF'ed samples of (a) In939 and (b) In939+TiB_2 under varying laser power and scan speed. The images demonstrate that the addition of TiB_2 particles notably inhibits cracking, as evident in the cross-sectional SEM images. Cracks and porosities are highlighted using red and yellow arrows, respectively. (c) The relative densities of all samples. (For interpretation of the references to colour in this figure legend, the reader is referred to the Web version of this article.)

In939+TiB_2 composites exhibited both irregular and spherical pores, suggesting the coexistence of gas porosity and lack-of-fusion porosity. The porosity dimensions of the In939+TiB_2 samples reveal a clear dependence on laser power and scanning speed. At lower laser power, the pore size increased with increasing scanning speed. For example, in P1, pores ranged between 15 and 20 μm, while in P4, the pore size reached up to 140 μm, indicating insufficient energy input at high scanning speeds, leading to a lack of fusion. At higher laser power, porosity was significantly reduced. In P5 and P6, trace amounts of pores were observed, with sizes remaining below 10 μm, reflecting improved melt pool stability and better powder fusion. However, at the highest scanning speed (P8), the pore size increased slightly to approximately 30 μm. These results demonstrate that increasing laser power improves densification and reduces porosity, while the scanning speed must be carefully optimized to avoid defects caused by insufficient melting or excessive energy input. Therefore, the new optimal volumetric energy input conditions for this composite were determined to be higher than those for pure In939, identified as P6 (VED: 125 J/mm^3) and hereafter referred to as In939+2TiB_2. It is believed that TiB_2 particles on the surface of the Inconel 939 particles increased the effective thermal conductivity of the blended powders [13,14]. However, further characterizations of this study revealed the decomposition of TiB_2 during LPBF. The energy used to decompose TiB_2 into Ti and B might have led to an increase in the total VED to achieve high-density In939+TiB_2 samples. As a result, a higher laser energy density was required to achieve high-density In939+TiB_2 compared to pure In939. Consequently, it is clear that incorporating TiB_2 has a more profound effect on crack inhibition than merely altering LPBF conditions in pure In939.

X-ray CT analysis was conducted on samples of In939 and In939+2TiB_2 to provide a detailed examination of the distribution of cracks and pores following the LPBF process (Fig. 5). The 3D reconstruction of the In939, as shown in Fig. 5(a), reveals significant cracks at first glance. Fig. 5(c) presents a maximum Feret diameter distribution of cracks, indicating a maximum crack length of 512 μm extending along the build direction. Conversely, the 3D reconstruction of the In939+2TiB_2 sample, as seen in Fig. 5(b), displays no cracks and only spherical pores large enough (maximum 68 μm) to be visible at the captured resolution. As a note, Supplementary Fig. 3 shows an SEM image of In939+5TiB_2, which is also free of cracks. The pore size distribution of this In939+2TiB_2 sample, provided in Fig. 5(d), confirms this finding, showing a collection of pores with maximum Feret diameters in the tens of microns range. It is important to note that pores of similar size, shape, and number density were also observable in the pure In939 sample, along with the cracks. Overall, approximately 2.5 mm^3 of In939 analyzed in the described reconstruction exhibited a relative density of 99.86%, while adding TiB_2 increased it to 99.94%.

3.3. *Microstructures of as-printed In939+TiB_2 composites*

XRD analysis was performed to examine the overall phase distribution in In939 and In939+2TiB_2. Fig. 6(a) displays XRD scans of various Inconel samples: as-received In939 powder, blended In939+2TiB_2 powder, In939, and In939+2TiB_2. In all specimens, the dominant phase is the face-centered cubic (FCC) gamma nickel-chromium (Ni, Cr) phase (γ). Additionally, In939 reveals the XRD peak of MC, indicating the formation of carbides in LPBF-processed In939, a finding commonly reported in the literature as well [5,41]. Conversely, In939+2TiB_2 showed peaks for CrB and CrB_2, but not for MC or TiB_2, which differs from the XRD patterns of In939 and blended In939+2TiB_2 powders. The Cr-based boride peaks seen in the XRD plot were also confirmed by EELS analysis, which shows overlapping Cr and B signals (Fig. 6(b)). Therefore, it is inferred that the nano TiB_2 particles decomposed into Ti and B during LPBF, and the free B reacted with Cr to form Cr-based borides. The authors of this study have previously observed similar phenomena during LPBF of ZrB_2 and SiC-doped In718 [17,42]. In one study, (Nb, Ti)-based carbides and silicides formed due to SiC decomposition during LPBF of In718+SiC [17]. In another study, ZrB_2 transformed into (Co, Mo, Nb)-based borides in In718 during LPBF [42].

In Fig. 7, backscattered electron (BSE) mode SEM images and corresponding EDX mapping obtained from In939 are presented. In939 exhibits columnar grains extending along the build direction (Fig. 7(a)). Additionally, the morphology of the cracks shows primary dendrite

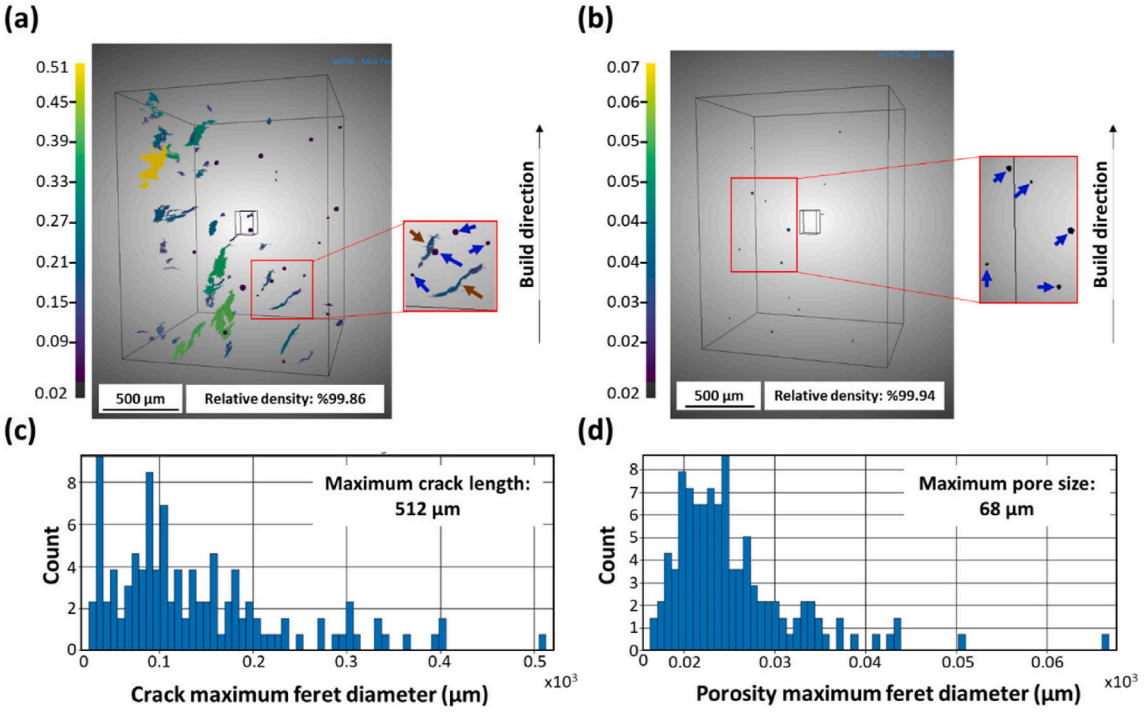

Fig. 5. (a–b) 3D reconstructions displaying pores and cracks formed during printing of In939 and In939+2TiB_2. (c–d) Defect distribution plots of the respective samples.

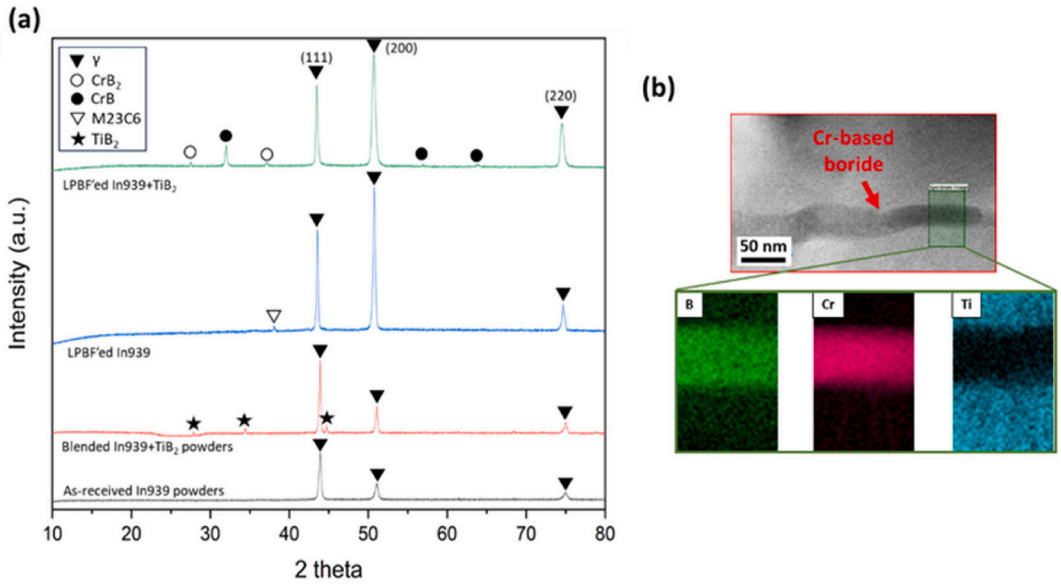

Fig. 6. (a) XRD analysis obtained from raw In939 powder, In939+2TiB_2 powder, In939, and In939+2TiB_2. (b) STEM/EELS analysis obtained from In939+2TiB_2 samples confirming the formation of Cr-based borides after LPBF.

arms, indicating the formation of solidification cracking in pure In939 (the region in red square in Fig. 7(a) and Supplementary Fig. 2) [4]. Solidification cracks typically form during the terminal stages of solidification when insufficient liquid remains to accommodate shrinkage strains, resulting in irregular and misaligned crack surfaces containing dendritic features. These observations are consistent with the well-established characteristics of solidification cracking described in the literature [40]. Therefore, the observed cracks in pure In939 are conclusively identified as solidification cracks, further supported by the presence of dendritic features on the fracture surfaces [40]. Moreover, higher magnification BSE-SEM images of the pure In939 sample display darker regions, approximately 1–2 μm thick, extending along the build direction (regions in yellow dashed squares in Fig. 7(b) and (c)). These regions are enriched with Ti, Nb, Ta, and C, as confirmed by the SEM/EDX mapping shown in Fig. 7(d). Thus, it can be inferred that the elongated dark regions are the characteristic interdendritic areas formed during the LPBF of In939 [5]. There are also small bright particles, indicated by blue arrows (<500 nm), predominantly located in the interdendritic regions. These particles exhibit stronger C signals, along with Ti, Nb, and Ta, and are presumed to be part of the MC-type phase identified in the XRD analysis. Therefore, it is likely that Ti-, Nb-, and Ta-rich carbides formed in the interdendritic regions due to the segregation of Ti, Nb, Ta, and C in the liquid during the later stages of solidification. On the other hand, In939+2TiB_2 sample displays equiaxed grain morphologies (Fig. 7(e)) dissimilar to those of In939 (Fig. 7(a)). This suggests that the addition of TiB_2 significantly influenced the microstructure of In939 during LPBF. This effect is more evident in higher magnification BSE-SEM images (Fig. 7(f and g)). The microstructure of In939+2TiB_2 exhibits an even distribution of dark and bright phases, indicated by red and green arrows, respectively. According to the SEM/EDX mapping shown in Fig. 7(h), the dark phases exhibit strong Cr signals, while the bright regions show strong Ti and Nb signals. Particularly, it can be observed that Ti forms the boundaries of solidification cell structures, which measure approximately ~1.6μm. In addition, the Cr-rich and Nb/Ti-rich regions are adjacent to each other and form a network-type distribution throughout the microstructure.

Following the SEM analysis, STEM characterizations were carried out to understand the microstructural aspects in more detail. Fig. 8 displays dark-field STEM and corresponding EDX characterizations performed on In939. Firstly, Ti-, Nb- and Ta-based carbides, highlighted in yellow dashed circles, are detected in higher resolution and their size varies between 50 and 100 nm (Fig. 8(a) and Supplementary Fig. 4). It is also important to mention that no other precipitates were observed in In939 except the MC carbide precipitates. This is also confirmed by the SAED pattern captured from the γ region, as indicated by the brown point in Fig. 8(a). Furthermore, STEM/EDX results obtained from Supplementary Fig. 5 and Supplementary Table 1 confirm that the type of carbides appears to be MC-type carbides. Specifically, the SAED pattern only shows diffraction patterns belonging to the γ phase without any secondary diffraction patterns, indicating the non-existence of precipitates. On the other hand, the In939+2TiB_2 specimen shows a Cr- and B-rich phase region surrounded by Ti-enriched regions (Fig. 8(b)). This phase is confirmed to be the CrB_2 phase by the SAED pattern shown in Fig. 8(f). These precipitates are indicated by red arrows. Furthermore, STEM-EDX line analysis performed along the yellow line in Fig. 8(c) reveals the compositional gradient in the interface between CrB_2 and Ti-rich region, confirming the exchange reaction between TiB_2 and Cr during LPBF. Besides that, it is evident that the CrB_2 region and matrix have a good interface bonding thanks to the Ti gradient at the interface. Lastly, In939+2TiB_2 specimens do not show any precipitates such as delta, sigma, and R, as proven by the SAED pattern obtained from γ phase in In939+2TiB_2.

Fig. 9 presents the EBSD inverse pole figure (IPF) maps, pole figures (PF), and grain size distribution plots of In939 and In939+2TiB_2. The IPF maps clearly demonstrate a significant reduction in grain size after the incorporation of TiB_2 into In939 (Fig. 9(a and b)). The PFs of In939 indicate that the undoped specimen has a strong cube texture of {100}< 001 > with a maximum texture intensity value of 14 (Fig. 9(c)). However, In939+2TiB_2 shows significantly lower texture intensity values in all directions compared to In939 (Fig. 9(d)). The grain sizes in the distribution plots represent the maximum Feret diameters measured from individual grains (Fig. 9(e)). This plot confirms a marked reduction in grain size for In939+2TiB_2, with an average grain size of 12.7 μm, substantially smaller than the average grain size of over 100 μm in In939. Furthermore, an IPF map shown in Supplementary Fig. 6 confirms the significant reduction in grain size achieved by the incorporation of TiB_2 particles when In939 and In939+TiB_2 are LPBF-processed under the same parameters (i.e., P6). Our findings reveal that the addition of TiB_2 particles promotes the formation of equiaxed grains in LPBF-processed In939, significantly altering the microstructural evolution during solidification. This behavior is attributed to multiple mechanisms arising from the decomposition of TiB_2 particles and their

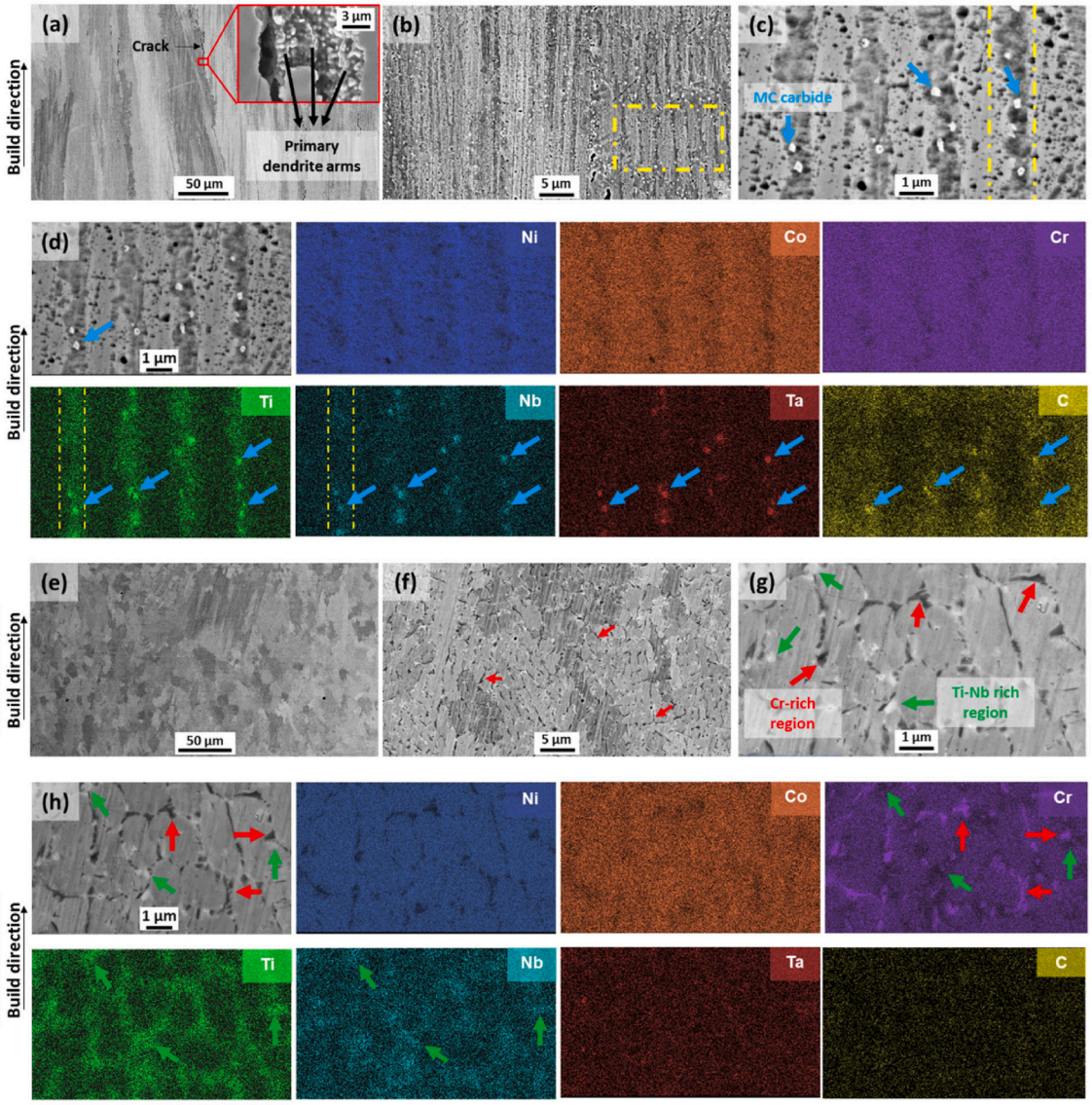

Fig. 7. (a–c) BSE-SEM images obtained from In939 sample, (d) SEM-EDX mapping analysis obtained from In939 sample. Please note that blue arrows indicate Ti-, Nb- and Ta-based carbides, and Ti-Nb rich zones are highlighted by dashed yellow squares. (e–g) BSE-SEM images obtained from In939+2TiB_2 sample, (h) SEM-EDX mapping analysis obtained from In939+2TiB_2 sample. Please note that the Cr-rich and Ti-Nb rich are indicated by red and yellow arrows, respectively. (For interpretation of the references to colour in this figure legend, the reader is referred to the Web version of this article.)

subsequent impact on the solidification path. During the LPBF process, TiB_2 particles decompose, releasing boron, which reacts with chromium to form CrB_2 and other Cr-rich boride phases. These in-situ-formed borides act as highly effective heterogeneous nucleation sites, reducing the energy barrier for nucleation and facilitating the formation of equiaxed grains near the solid-liquid interface. By disrupting the unidirectional growth of columnar grains, these borides alter the typical solidification dynamics observed in pure In939. The effect of CrB_2 precipitates extends beyond nucleation, influencing the local solidification conditions in several critical ways. First, the high thermal conductivity of CrB_2 precipitates leads to a more uniform temperature distribution across the melt pool, mitigating steep thermal gradients that drive columnar grain growth. Second, the localized enrichment of Ti and B near the solid-liquid interface enhances constitutional undercooling, promoting simultaneous nucleation events and supporting the development of equiaxed grains. Third, CrB_2 particles act as physical barriers to grain boundary migration, exerting a Zener pinning effect that stabilizes the equiaxed grain morphology by preventing the dominance of columnar growth. The EBSD results provide clear evidence of these phenomena, showing a refined, equiaxed grain structure in In939+TiB_2 with significantly reduced texture intensity compared to the columnar grain structure of pure In939.

3.4. *Exploring the mechanical behavior of TiB_2-doped composites*

Tensile and microhardness tests were conducted to evaluate the mechanical properties of the TiB_2-doped composite. As a result, the addition of the TiB_2 significantly improved tensile strength in In939 with a satisfactory fracture strain (13–15 %). Accordingly, the average hardness was observed to be 354 HV for In939 and rose to 535 HV for In939+2TiB_2, indicating a ~50 % increase in hardness for the composite (Supplementary Fig. 7). Tensile stress-strain curves of In939, In939+2TiB_2 and In939+5TiB_2 are provided in Fig. 10(a). Both In939+2TiB_2 and In939+5TiB_2 show 1.5 times more yield strength (σ_{YS}) and ultimate tensile strength (σ_{UTS}) compared to In939. Although the observed elongation of In939+2TiB_2 is around 13–15 % and lower compared to In939 (which was around 30–35 %), this level of ductility is still considered acceptable for a particle-reinforced superalloy produced

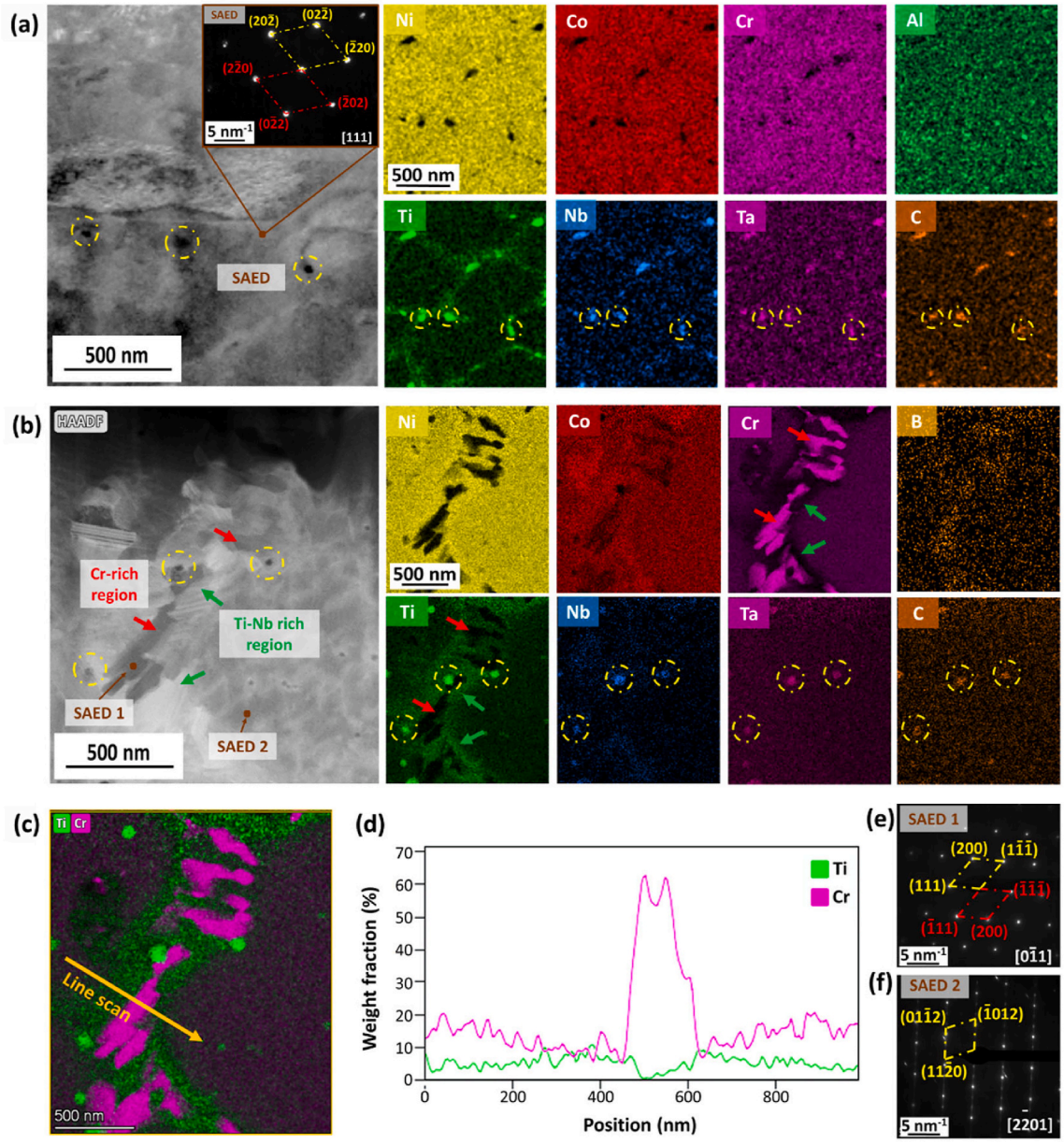

Fig. 8. (a) Darkfield STEM image and corresponding STEM/EDX mapping showing the elemental distribution in the microstructure of In939, (b) Darkfield STEM image and corresponding STEM/EDX mapping of In939+2TiB$_2$,showing the Cr-based boride and surrounding Ti-rich zone revealing the exchange reaction between TiB$_2$ and Cr, (c–d) STEM/EDX mapping of In939+2TiB$_2$.and corresponding line scan analysis showing the concentration profile of Cr and Ti along exchange reaction zone, (e) SAED pattern obtained from gamma matrix revealing the non-existence of other precipitates in In939+2TiB$_2$. (i.e., gamma prime), and (f) SAED pattern obtained from Cr and B rich region revealing the formation of CrB$_2$ in In939+2TiB$_2$. Please note that the Cr-rich and Ti-Nb rich are indicated by red and green arrows, respectively. Besides, Ti-, Nb-, and Ta-based carbides are highlighted by dashed yellow circles. (For interpretation of the references to colour in this figure legend, the reader is referred to the Web version of this article.)

by LPBF. Another interesting result is that In939+5TiB$_2$ exhibits very low ductility despite having similar strength to In939+2TiB$_2$. This suggests that adding 5 vol% TiB$_2$ leads to excessive embrittlement in the composite at RT. Fig. 10(b and c) provides σ_{YS} and σ_{UTS} comparison plots of several LPBF processed In718 composites and LPBF'ed + heattreated In939 [5,17,43–47]. σ_{YS}, σ_{UTS} and tensile strain of non-heat treated In939+2TiB$_2$ are higher than those of LPBF'ed and heat-treated In718+SiC, In718+TiC and In939, which used to be the highest strength-ductility pair among superalloys [4,5,17,43]. Furthermore, the tensile properties of the as-printed In939+2TiB$_2$ exceed those of the as-printed In939+Si alloys and LPBF In738 and In713LC, with no cracks observed in either instance [4,48,49].

Fig. 11(a–d) presents SEM images taken from the fractured surfaces of In939 and In939+2TiB$_2$. The fracture surface of the LPBF-optimized In939 alloy exhibits prominent voids, denoted by white arrows, and dimples, highlighted by yellow circles, indicative of substantial plastic deformation. In contrast, the fracture surface of In939+TiB$_2$ displays regions of flat topography alongside dimples, implying a fracture mechanism that is not solely ductile but also partially brittle (indicated by red lines). This is within expectations since the elongation of In939 decreased by 50% after TiB$_2$ addition. Fig. 11(e) presents a schematic representation of the microstructure of In939+2TiB$_2$ and the interaction between dislocations and intermetallic compounds. As depicted in Fig. 11(f–h), CrB$_2$ and MC carbides demonstrate effective impediments to dislocation movement, thereby enhancing the strength of the material.

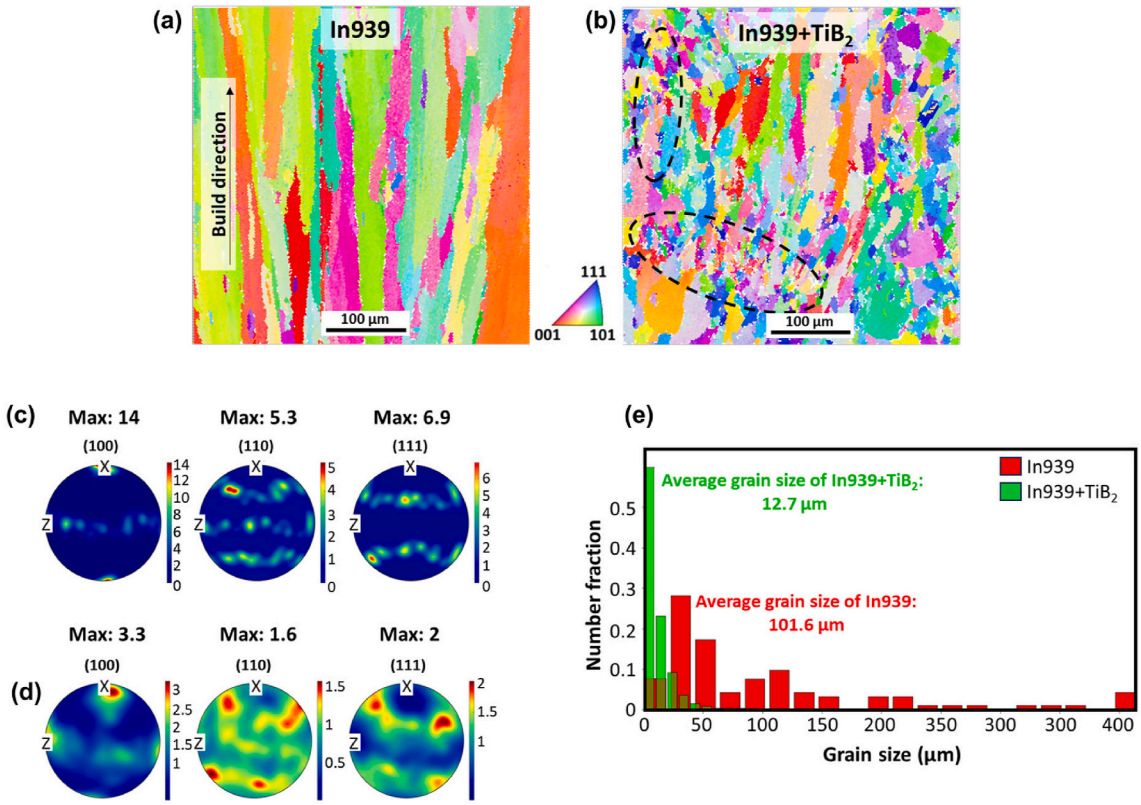

Fig. 9. EBSD results for In939 and In939+2TiB_2: (a, b) inverse pole figure (IPF) maps of In939 and In939+2TiB_2, respectively; (c, d) corresponding pole figure (PF) maps; and (e) grain size distribution plot. Equiaxed fine grains are highlighted with black dashed lines.

Considering the widespread high-temperature applications of Ni-based superalloy, we investigate the high-temperature behavior of the composites through tensile tests conducted at 800 °C and 850 °C. Compared to the high-temperature behavior of pure In939, the addition of TiB_2 was found to further enhance the high-temperature tensile properties. This demonstrates that the strengthening effect of TiB_2 addition is effective even at elevated temperatures. As depicted in Fig. 12(a), pure In939 is observed to experience premature failure in the elastic region. This phenomenon is likely due to the printing defects, e.g. pre-existing cracks with lengths up to 0.5 mm and widths up to 0.01 mm within the In939 samples, as shown in Fig. 4. Given the ~0.23 mm thickness of the samples for high-temperature tensile testing, it is inferred that these pre-existing cracks could easily lead to premature failure. Fig. 12(c) and (d) present the fracture surfaces of In939 and In939+5TiB_2 after testing at 800 °C. In the case of In939+5TiB_2, the observations unveil cleavage fracture characteristics as well as indications of ductile fracture, as evidenced by void and dimple formation. In contrast, In939 exhibits surface features indicative of purely brittle fracture, marked by rapid crack propagation from pre-existing cracks. The high-temperature properties of In939+5TiB_2 composite are summarized in Table 3 and Fig. 12(b), alongside the corresponding properties of In939 from the literature [2,5,9]. Fig. 12(b) demonstrates that In939+5TiB_2 possesses superior yield strength (YS) and ultimate tensile strength (UTS) at elevated temperatures. Notably, at 800 °C, the YS, and UTS of In939+5TiB_2 surpass those of both LPBF'ed and LPBF'ed + heat-treated In939 [5]. Compared to electron beam melted (EBM) In939 tested at 700 °C [2]. In939+5TiB_2 exhibits higher YS and comparable UTS at 800 °C, despite the 100 °C increase in the testing temperature. Lastly, it is also striking that the YS and UTS of In939+5TiB_2 at 800 °C are higher than those of cast + aged In939 at 750 °C [9].

One notable finding is that while the In939+2TiB_2 composite showed the best tensile properties at room temperature, the In939+5TiB_2 composite outperformed it at elevated temperatures. To understand these contrasting results, TEM analysis was conducted on the sample fractured at 800 °C, and the findings are presented in Fig. 13. For the In939+5TiB_2 sample, the network of Cr-rich precipitates remained relatively intact even after fracturing at 800 °C (Fig. 13(a)), whereas these microstructural features were almost absent in the In939+2TiB_2 sample (Fig. 13(b). This suggests that the strengthening mechanism from the microstructural features in the In939+2TiB_2 composite is effective at room temperature but loses its efficacy at high temperatures. In contrast, the addition of 5 vol% TiB_2 results in a composite with superior strength, while maintaining moderate ductility at elevated temperatures, which are sufficient for structural applications such as turbine shrouds, nozzle guide vanes, or combustor liners requiring a balance between strength and deformability. The superior high-temperature tensile properties of the 5TiB_2 composite compared to those of the 2TiB_2 can be attributed to the enhanced thermal stability of its CrB_2 network. The higher TiB_2 content in the 5TiB_2 alloy ensures sufficient B solute availability in the matrix during solidification, promoting the formation of a more complete and interconnected CrB_2 network. This robust network, supported by strong covalent bonding between B and Cr, effectively resists thermal dissolution and coarsening at elevated temperatures, thereby preserving its structural integrity. In contrast, the lower B content in the 2TiB_2 alloy results in a less stable CrB_2 network, reducing its strengthening contribution under high-temperature conditions.

4. Discussion

4.1. Crack inhibition and cracking mechanisms

It is well-known that the formation of equiaxed grains significantly alleviates texture and promotes a random distribution of residual stresses in LPBF-processed alloys [30]. The weaker texture intensity, along with the smaller grain size (Fig. 9(b) and (d)), likely contributes to

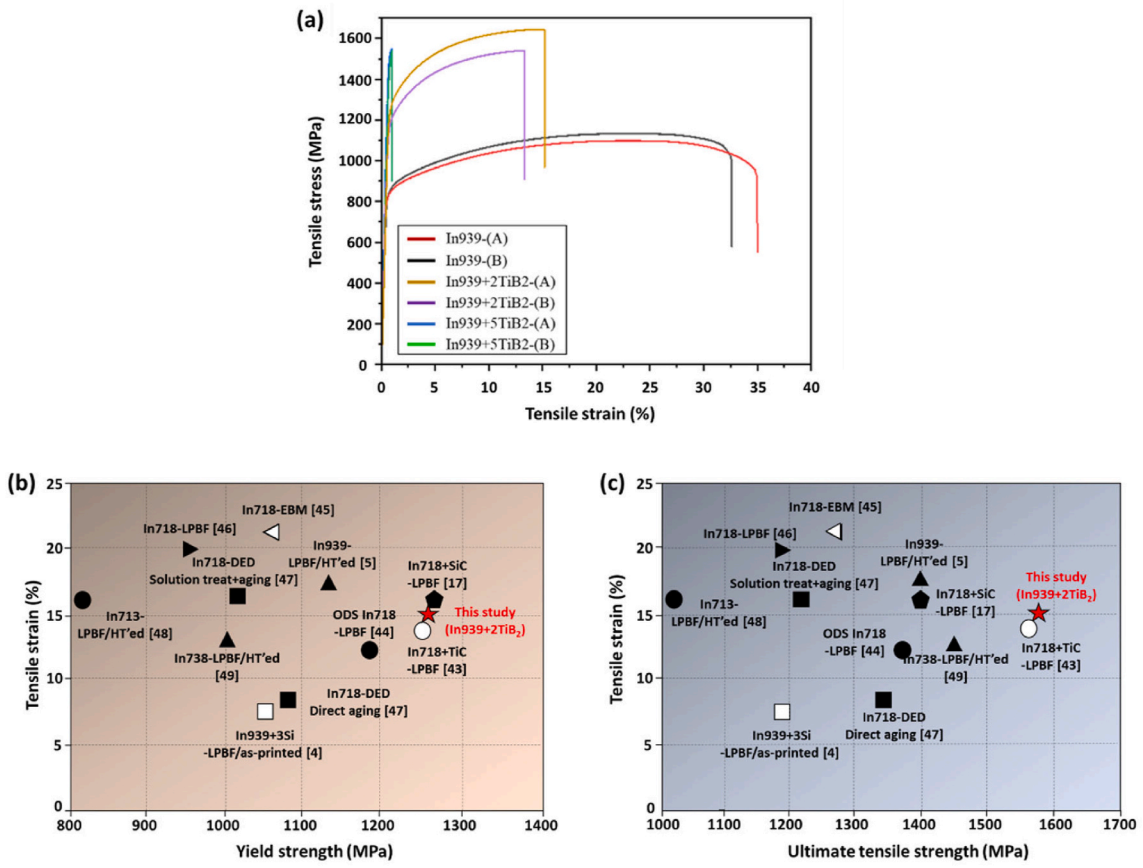

Fig. 10. (a) Room temperature tensile stress-strain curves of pure In939 and In939 + TiB_2 and (b–c) Tensile strain vs. YS (MPa) and Tensile strain vs. UTS (MPa) of several AM In718 alloys and composites, and LPBF-processed In939 from the literature.

a more uniform macro-scale stress distribution in In939+2TiB_2, enhancing crack resistance by reducing stress concentration points that typically facilitate crack initiation. Another notable observation is the substantially different KAM distribution patterns (Fig. 14(a) and (b)). Specifically, larger KAM zones in In939 tend to extend along the build direction with a stripe pattern, while larger KAM zones in In939+2TiB_2 exhibit a more random distribution, overlapping with the equiaxed grain zones (white dashed region).

The density of geometrically necessary dislocations (GNDs) can be correlated with KAM, providing insights into the accumulation of residual stresses in LPBF-processed samples through the following equation [50]:

$$\rho_{GND} = \frac{2\varphi}{\mu b} \tag{6}$$

where ρ_{GND} is the average GND density, φ represents the local average misorientation, μ is the step size for the EBSD test (2 μm), b is the Burgers vector (b = 0.25 nm). The average KAM values of In939 and In939+2TiB_2 are 0.88 and 0.98, respectively. Based on the formulation, the calculated geometrically necessary dislocation (GND) densities for In939 and In939+2TiB_2 are 0.61 × 10^{14} m^{-2} and 0.69 × 10^{14} m^{-2}, respectively. These results reflect localized micro-scale misorientations and dislocations that contribute to enhanced strength without creating detrimental residual stresses. Therefore, it is hypothesized that this distinction between macro-scale and micro-scale stress distribution helps clarify the observations, as In939+TiB_2's refined grain structure and random orientation reduce macro-scale stress concentrations, while localized microstructural heterogeneities can enhance the overall material strength. In this context, subsequent characterizations are aimed at more thoroughly elucidating the crack inhibition mechanism.

Fig. 15 presents SEM/EDX mapping and EBSD characterizations performed on cracked regions in In939. Fig. 15(a) clearly shows segregation of multiple elements near the crack zones, particularly Ti, Nb, Ta, C, Al, and O, indicating solidification cracking during LPBF of unreinforced In939. The red arrows in Fig. 15(a) point to accumulations of Ti-, Nb-, and Ta-rich carbides around the cracks. Such clustering can disrupt local feeding of liquid during the final stages of solidification and act as stress concentrators, promoting crack initiation and propagation [29]. Additionally, yellow-arrow regions exhibit strong Al and O signals, suggesting oxide formation at or near grain boundaries. Oxide films can hinder grain coalescence and have been linked to cracking mechanisms such as dynamic embrittlement (DE) and stress-assisted grain boundary oxidation (SAGBO) [28], particularly under conditions of elevated temperature and tensile stress at crack tips. Moreover, EBSD analysis (Fig. 15(c–f)) reveals that cracks propagate preferentially along high-angle grain boundaries (HAGBs), confirming their intergranular nature. High-resolution IPF maps show fine grains along crack paths (Fig. 15(f)), which may have formed from backfilling of residual liquid or solute-rich melt during solidification, followed by carbide and oxide clustering. These microstructural features suggest a failure mechanism governed not just by solute segregation, but also by insufficient ductility and cohesion in the terminal solidification range.

To better understand these observations, the thermomechanical aspects of solidification cracking must be considered. During LPBF, rapid solidification results in an extended mushy zone, where semi-solid regions must accommodate thermal contraction and residual stresses. If the terminal solidification range is broad, thin liquid films persist between dendrites for a longer duration, weakening the mushy zone and increasing its susceptibility to cracking. In this context, we assessed the solidification behavior of In939 and In939+TiB_2 using thermodynamic

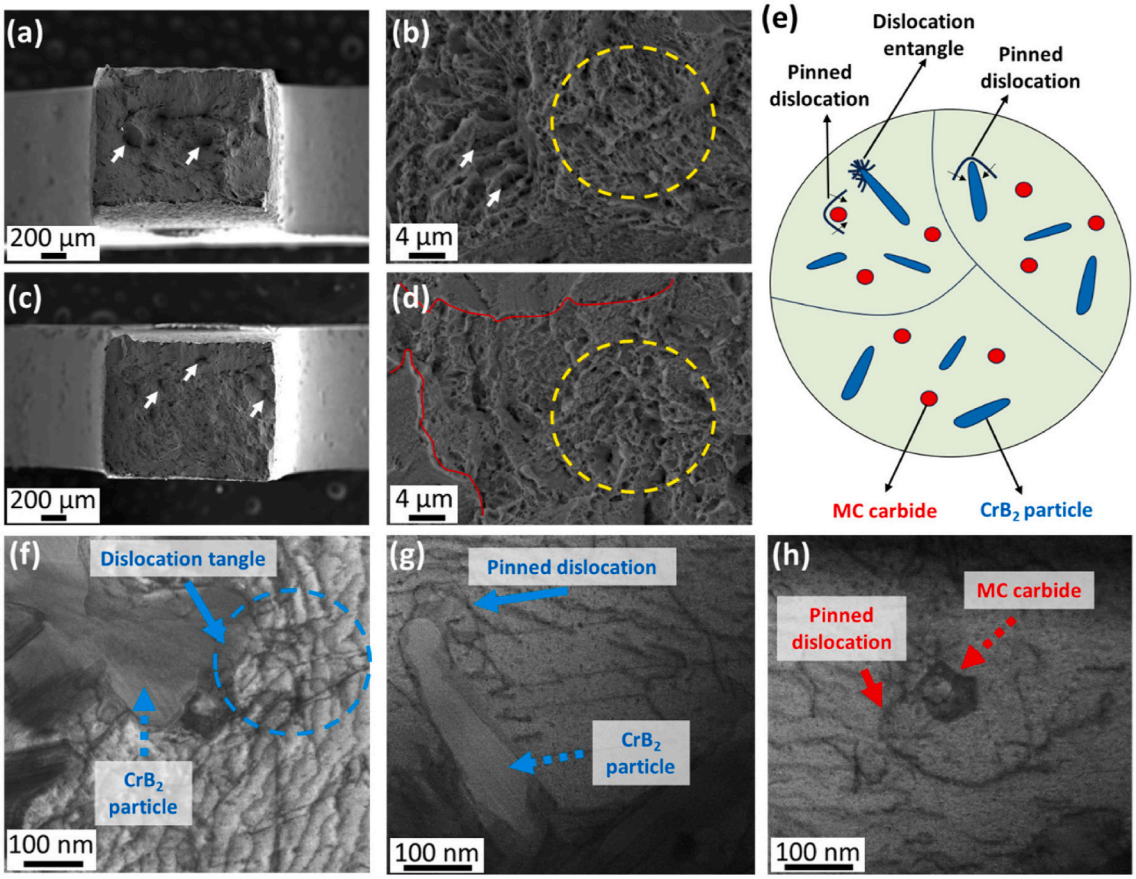

Fig. 11. SEM images taken from the fracture surfaces of (a–b) In939, (c–d) In939+2TiB_2. (e) Schematic illustration depicting interactions between CrB_2 and MC particles with dislocations in the composite after RT tensile testing. (f) STEM image revealing the interaction of dislocations with CrB_2 and the matrix after LPBF. (g–h) STEM images displaying dislocation interactions with CrB_2 and MC particles following RT tensile testing.

simulations. Scheil-Gulliver results (Fig. 16) show that the In939+2TiB_2 sample has a ~70 °C narrower terminal freezing range (f_s = 0.9 to 1.0) compared to undoped In939. According to Kou's criterion [40], this narrower range enhances dendrite bridging and reduces exposure to strain-sensitive semi-solid regions, thereby lowering the risk of cracking. The total freezing range is also reduced by ~10 °C in the TiB_2-doped alloy. These findings suggest a stronger and more coherent mushy zone in the composite. The solidification paths under both equilibrium and non-equilibrium (Scheil) conditions are shown in Fig. 16(a and b). While equilibrium calculations predict the formation of σ, μ, and η phases, these phases are not observed in LPBF-processed microstructures, likely due to the high cooling rates and kinetic constraints. Scheil simulations, despite not accounting for back-diffusion in the solid and possibly overestimating segregation, still reliably reflect trends in micro-segregation [51]. For instance, enrichment of Ti and Ta in the final liquid is predicted in both alloys and confirmed by EDS in Figs. 7 and 8, validating the model's qualitative accuracy. Scheil simulations also predict early TiB_2 precipitation, represented as MB_2-type borides in Thermo-Calc. However, TiB_2 is not observed in the final microstructure, indicating decomposition during processing. This is likely due to non-equilibrium melt-particle interactions, leading to the formation of Cr-rich borides, which are confirmed by SEM/EDS and STEM/EDS. These secondary borides likely act as heterogeneous nucleation sites, refining the grain structure. This mechanism is consistent with observations by Martin et al. [52] in Zr-doped Al alloys, where Al_3Zr particles suppressed cracking and promoted equiaxed grains. Similarly, we propose that B released from decomposed TiB_2 reacts with Cr to form these borides, which pin grain boundaries and facilitate equiaxed solidification.

Grain structure also plays a critical role. Intergranular cracking is exacerbated in alloys with large columnar grains and strong texture, which concentrate thermal stresses along specific crystallographic planes. In contrast, equiaxed and randomly oriented grains are more effective in distributing stresses during solidification. EBSD analysis confirms that In939+2TiB_2 exhibits a finer and less textured grain structure compared to pure In939 (Fig. 9(d)). This refinement, along with the presence of potential heterogeneous nucleation sites provided by in situ formed borides, results in increased grain boundary density and improved strain accommodation during the final stages of solidification. In summary, the observed reduction in solidification cracking in In939+2TiB_2 can be attributed to a combination of: i) reduced terminal freezing range (improved mushy zone strength), ii) a finer and more equiaxed grain structure (enhanced strain accommodation), iii) suppression of detrimental elemental segregation patterns (e.g., carbide/oxide clustering at HAGBs), and iv) potential grain boundary pinning or nucleation effects from Cr-rich borides. Collectively, these mechanisms contribute to a more stable solidification front and enhanced resistance to intergranular cracking during LPBF.

4.2. *Strengthening mechanisms*

The exceptional room-temperature strength of In939+2TiB_2 can be attributed to various strengthening mechanisms. In general, the strengthening mechanisms in reinforced composite materials can be understood by considering two aspects: (i) load transfer strengthening, based on continuum mechanics, and (ii) micromechanical strengthening mechanisms, which involve the interaction between microstructural features and dislocations [53,54]. The load transfer strengthening effect

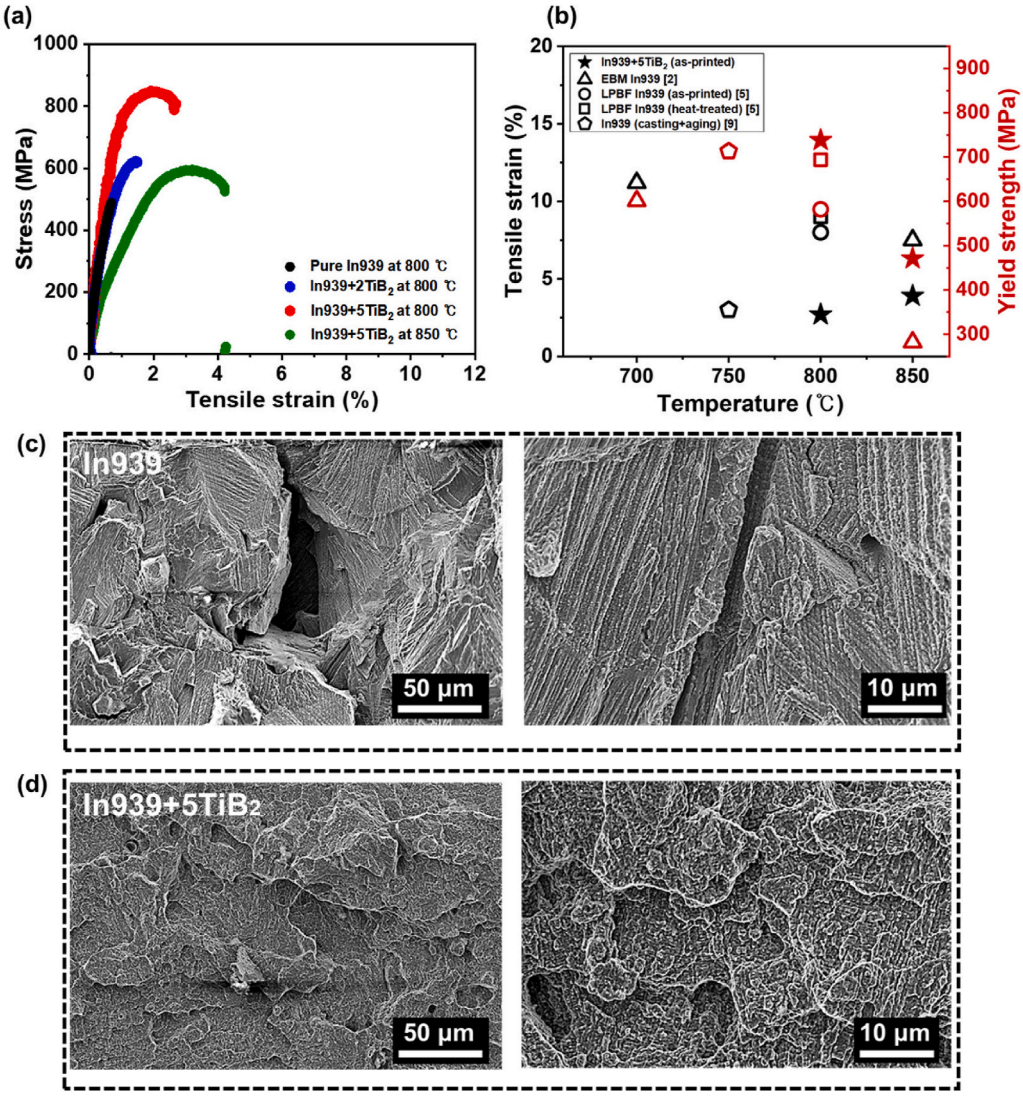

Fig. 12. (a) Representative stress-strain curves for In939 and In939+5TiB_2 at 800 °C and 850 °C; (b) Superior high-temperature strength of In939+5TiB_2 compared to other In939 alloy as reported in the literature; Fracture surfaces of (c) In939 and (d) In939+5TiB_2 at 800 °C.

Table 3
Comparison of 800 °C and 850 °C tensile properties of In939+5TiB_2 and other In939 materials from the literature.

Material	Condition	Temp. (°C)	YS (MPa)	UTS (MPa)	EL (%)
In939 [2]	EBM	700	601	843	11
		850	282	397	7.5
In939 [5]	LPBF	800	582	775	8
	LPBF + heat-treated	800	694	720	9
In939 [9]	Cast + aged	750	713	825	3
In939+5TiB₂ (This study)	*LPBF (as-printed)*	*800*	*734 ± 9*	*845 ± 2*	*2.5 ± 0.4*
		850	*465 ± 6*	*597 ± 4*	*3.9 ± 0.4*

can be estimated using the modified shear-lag model, which accounts for the volume fraction (V_f) and aspect ratio (s) of the reinforcement particles [54]:

$$\sigma_{y,composite} = \sigma_{y,matrix}\left[\frac{V_f(s+2)}{2} + (1 - V_f)\right]. \quad (7)$$

As indicated by the model, when reinforcement particles have a low volume fraction and low aspect ratio (i.e., are not fiber-shaped), their contribution to load transfer strengthening becomes limited [53,54]. In this study, the CrB_2 particles are present at a volume fraction below 2 % and exhibit a relatively low aspect ratio compared to fiber reinforcements. Therefore, the load transfer strengthening effect is considered negligible in this system. Consequently, the strengthening of the In939+TiB_2 composite is expected to be dominated by micromechanical mechanisms related to its unique microstructural features and their interactions with dislocations. By incorporating the strengthening effects arising from microstructural features of the composite into the yield strength of pure In939, the superior strength of the In939+TiB_2 composite can be rationalized as (Eq. (8)).

$$\sigma_{y,In939+TiB2} = \sigma_{y,In939} + \Delta\sigma_{strengthening\ effect.} \quad (8)$$

Compared to pure In939, the key microstructural characteristics observed in the In939+TiB_2 composite can be summarized as follows: i) Fine grain structure, ii) Well-defined Ti-rich cellular boundaries, ii) The presence of CrB_2 ceramic particles. One important note is that strengthening due to MC carbides impeding dislocation motion is already reflected in the yield strength of pure In939, since MC carbides are also present in the pure alloy.

The first dominant mechanism is grain boundary strengthening. The

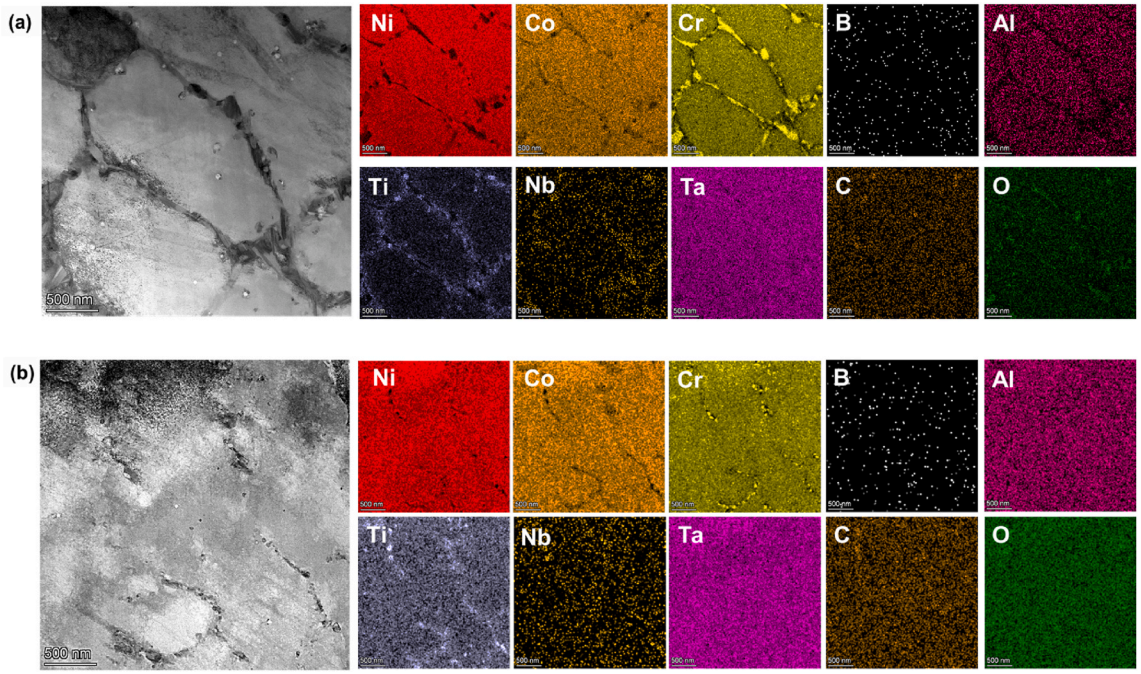

Fig. 13. BF-TEM image and STEM-EDS maps showing the distribution of precipitates in (a) In939+5TiB_2 and (b) In939+2TiB_2 deformed at 800 °C.

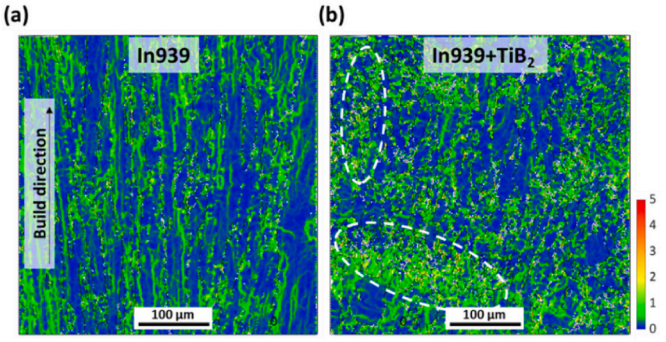

Fig. 14. Kernel average misorientation (KAM) map of (a) In939, (b) In939+2TiB_2.

grain size of In939+TiB_2 ($d \sim 12.7\ \mu m$) is significantly lower than that of pure In939 ($d \sim 101.6\ \mu m$), as previously shown in Fig. 8(g). Therefore, grain refinement may contribute to strength enhancement in accordance with the renowned Hall-Petch relationship [55]:

$$\Delta\sigma_{\mathrm{Hall-Petch}} = k_{HP}\left(d_{\mathrm{In939+TiB2}}^{-\frac{1}{2}} - d_{\mathrm{In939}}^{-\frac{1}{2}}\right). \quad (9)$$

where d is the grain size, and k_{HP} is the Hall-Petch coefficient (710 $MPa\sqrt{\mu m}$ [56]). In addition to the grain refinement effect, this study has demonstrated that TiB_2 particles undergo decomposition during the LPBF process, and the decomposed B subsequently reacts with Cr. Therefore, a contribution from solid-solution strengthening could also be expected. The effect of solid solution strengthening can be quantitatively assessed using Labusch's solution combined with the Gypen and Deruyttere model, as represented by Eq. (10) [55,57,58]:

$$\sigma_{SS} = \left[\sum_i (Z_L G)^{3/2}\left(\alpha\delta_i + \eta_i'\right)^2 c_i\right]^{2/3}. \quad (10)$$

where Z_L is a constant equal to 1/550, G denotes the shear modulus of the alloy ($G = \frac{E}{2(1+\nu)}$), α is a dimensionless constant equal to 16 ($3 < \alpha < 16$ for screw dislocations, and $\alpha > 16$ for edge dislocations) [55,56], and c_i represents the atomic concentration of the solute. The lattice misfit (δ_i) can be estimated by $\delta_i = (r_i - r_{Ni})/r_{Ni}$ [56], where r_i is the atomic radius of the solute, and r_{Ni} is that of the solvent Ni. $\eta' = \eta/(1 + |\eta|/2)$, where η is the modulus misfit calculated as $\eta = (G_0 - G_B)/G_B$ [55]. The use of η' instead of η is intended to account for the relative change in shear modulus with solute concentration, adjusted by a correction factor [57]. G_0 is the shear modulus of the solute, and G_B is that of the base metal. The parameters of the solute element utilized for assessing solid solution strengthening are summarized in Table 4. The influence of TiB_2 addition on solid solution strengthening is quantified by considering the difference between In939 and In939+TiB_2:

$$\Delta\sigma_{SS} = \Delta\sigma_{SS,\mathrm{In939+TiB2}} - \Delta\sigma_{SS,\mathrm{In939}}. \quad (11)$$

The as-printed In939+TiB_2 demonstrates clear segregation of Ti atoms, forming the boundaries of the solidification cell structures, as depicted in Fig. 7(h). The compositional microsegregation associated with these cell features can significantly influence the overall material strength. Internal lattice strain arising from atomic size and elastic modulus differences between solute-enriched and solute-depleted regions generates coherent internal stresses, which impede dislocation motion and contribute to strengthening [67,68]. The effect of compositional microsegregation on strengthening can be estimated as [67]:

$$\Delta\sigma_{MS} = 0.57M(A\eta_a Y)^{\frac{1}{3}}(2\pi Gb/d)^{\frac{2}{3}}. \quad (12)$$

where M is the mean orientation factor (3.06), d is approximated as the mean cell size (1.6 μm) and Y is defined as $\frac{2G(1+\nu)}{(1-\nu)}$ [68]. The amplitude factor A, describing the compositional difference between the average Ti composition at the cell boundary (c_b) and the cell interior (c_i), is calculated as $A = \frac{c_b - c_i}{6}$ [68]. The lattice misfit, η_a, caused by the increase in lattice parameter (a) associated with elemental enrichment, is given by $\eta_a = \frac{d\ln a}{dc} = 0.000881\ at\%^{-1}$ for Ti in Ni-based superalloys [69]. While Ti segregation occurs in both the pure alloy and the composite, the enhanced strength in the composite is primarily attributed to the evolution of the spatial morphology of the Ti-segregated network. The

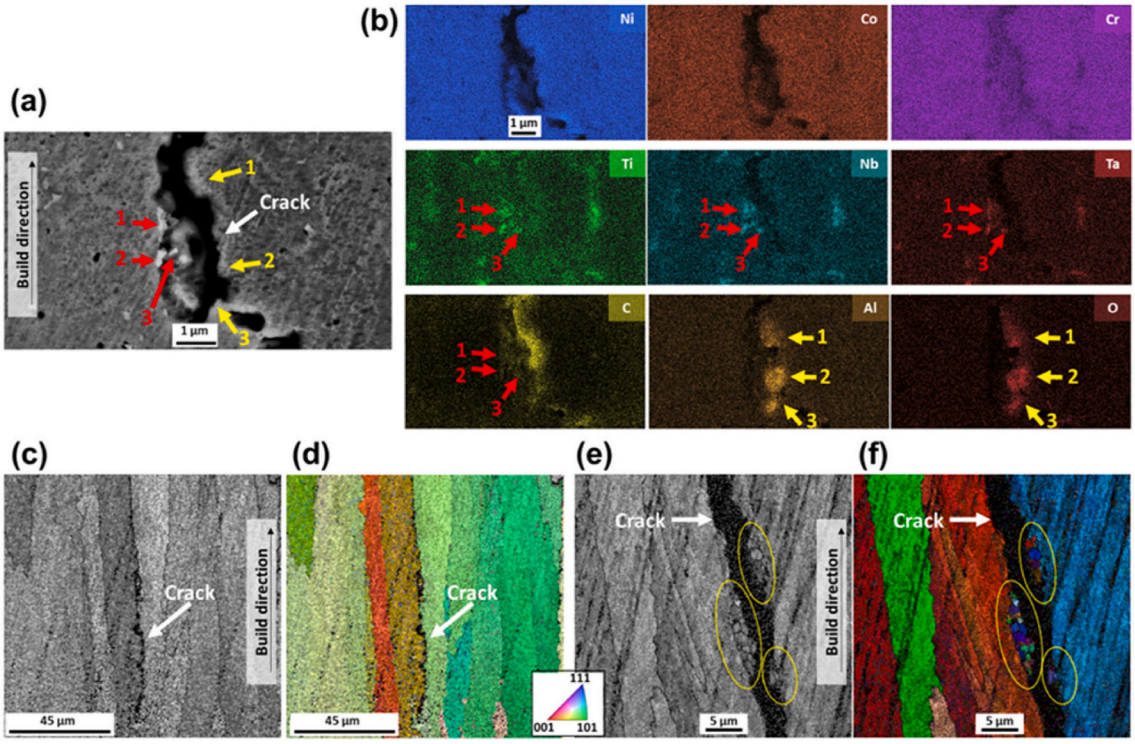

Fig. 15. (a,b) SEM/EDX analysis focusing on the cracked region, (c–f) inverse pole figure maps obtained from the cracking zones. Please note that Ti-, Nb-, Ta-based carbides and Al-based oxides are indicated by red and yellow arrows, respectively. (For interpretation of the references to colour in this figure legend, the reader is referred to the Web version of this article.)

CrB_2 precipitates, which are distributed along the cell boundaries, create a localized environment that facilitates the segregation of Ti. This physical confinement imposed by the CrB_2 network restricts the diffusion of Ti and concentrates its segregation along the boundaries, thereby sharpening the morphological definition of the cells. Furthermore, the CrB_2 particles stabilize the interface by acting as physical barriers to perturbations, thereby suppressing morphological instability and promoting more uniform solidification through interface pinning. This alteration promotes more distinct solute partitioning during solidification, resulting in sharper and more well-defined cell boundaries. This refinement leads to a more continuous and interconnected Ti-segregated network in the composite, which enhances mechanical interlocking and impedes dislocation motion more effectively.

The final strengthening contribution considered is the direct strengthening effect induced by CrB_2 particles. As discussed earlier, the CrB_2 particles tend to align along Ti-rich cell boundaries in a network-like configuration. This suggests that the dispersion strengthening effect through dislocation pinning may already be incorporated via dislocation interactions with the Ti-segregated cell structures. Therefore, in this context, only the coefficient of thermal expansion (CTE) mismatch strengthening is treated as a distinct additional contribution. The presence of CrB_2 particles at a size of several hundred nanometers can lead to the development of thermal residual stress due to the difference in the CTE between the particles and the matrix. The thermal residual stress can be large enough to result in an increase in the dislocation density [70]. This increase in dislocation density contributes to a further increase in the yield strength of In939+TiB_2, which can be expressed as a function of temperature as in Eqs. (13) and (14) [71]:

$$\Delta\sigma_{\mathrm{CTE}}(T) = \beta G_m(T) b \sqrt{\rho_{CTE}(T)}, \tag{13}$$

$$\rho_{CTE}(T) = \frac{12\Delta\alpha\Delta T V_{\mathrm{p}}}{b d_{\mathrm{p}}(1 - V_{\mathrm{p}})}. \tag{14}$$

Here, β is a constant of order 1, $\rho_{CTE}(T)$ is the dislocation density resulting from the CTE mismatch, $\Delta\alpha$ is the difference in CTE between CrB_2 (10×10^{-6}/K [72]) and the In939 matrix (13.99×10^{-6}/K [73]), ΔT is the difference between the solidification completion temperature (1075 °C, as determined from the Scheil curve) and the testing temperature, V_{p} is the volume fraction of the CrB_2 particles (1.86 %), and d_{p} is the approximated CrB_2 particle size (~260 nm). The volume fraction of CrB_2 is roughly estimated by assuming that all the Ti in the 2 vol% of TiB_2 is substituted with Cr. The theoretical model of CTE mismatch strengthening assumes a uniform distribution of dislocations, all of which contribute to strengthening. However, this assumption may not accurately reflect the behavior of a solution-hardened matrix [74]. Therefore, ρ_{CTE} calculated from Eq. (14) should be regarded as a reference for estimating the strengthening potential of CTE mismatch-induced dislocations, rather than as a representation of the actual dislocation density in the material.

The increases in yield strength attributable to the various strengthening mechanisms are summarized in Table 5. By summing the contributions from each mechanism according to Eq. (15), the predicted yield strength of In939+2TiB_2 is approximately 1275 MPa, starting from the base yield strength of pure In939 (842 MPa).

$$\sigma_{y,In939+TiB2} = \sigma_{y,In939} + \Delta\sigma_{\mathrm{GB}} + \Delta\sigma_{\mathrm{SS}} + \Delta\sigma_{\mathrm{MS}} + \Delta\sigma_{\mathrm{CTE}}. \tag{15}$$

This predicted value is slightly higher than the experimentally measured yield strength of In939+2TiB_2 (1256 MPa), but remains in close agreement. The simple linear summation approach is commonly used for predicting the yield strength of materials by considering various strengthening mechanisms [35,56,61]. However, this approach assumes that all mechanisms act independently and does not account for potential interactions among them. Moreover, other strengthening effects not explicitly addressed in this study—such as strengthening caused by solute atom segregation to dislocations [75]—may also contribute to the overall strength. As a result, while this approach provides a reasonable estimate, it may not be universally applicable. Further studies are warranted to develop a more rigorous and comprehensive predictive

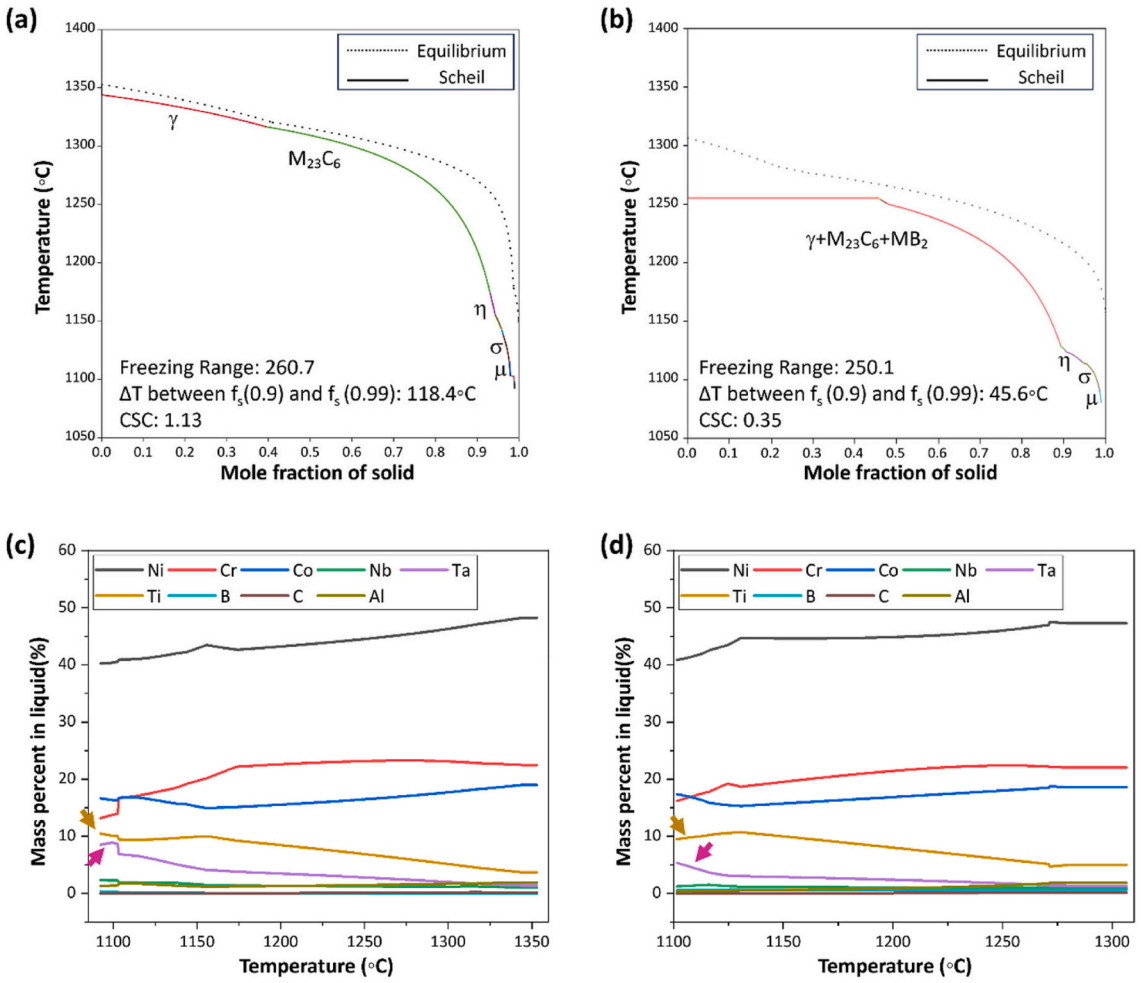

Fig. 16. Scheil solidification curves of specimens showing the difference between solidification patterns between undoped and TiB_2 doped In939: (a) In939, (b) In939+2TiB_2, and concentration profiles of elements in the liquid with respect to temperature derived from Scheil solidification data: (c) In939, (d) In939+2TiB_2.

Table 4
Parameters of the solute element for calculation on solid solution strengthening [59–66].

Element	Ni	Cr	Co	W	Nb	Ti	Ta	Zr	B
Elastic modulus (GPa)	223.3	251.6	201	415.8	103.6	110	188	77.8	403.6
Poisson's ratio	0.31	0.21	0.34	0.28	0.38	0.34	0.36	0.34	0.13
Atomic radius (nm)	0.117	0.13	0.118	0.15	0.156	0.148	0.158	0.164	0.084

Table 5
The calculated increment of yield strength contributed by various strengthening mechanisms.

Strengthening mechanism	$\Delta\sigma_{GB}$ (MPa)	$\Delta\sigma_{SS}$ (MPa)	$\Delta\sigma_{MS}$ (MPa)	$\Delta\sigma_{CTE}$ (MPa)
Yield strength increment	90	49	205	89

framework.

5. Conclusion

This study successfully demonstrated the fabrication of crack-free, high-strength In939-based metal matrix composites reinforced with TiB_2 using LPBF. The decomposition of TiB_2 during melting led to the in-situ formation of Cr-based boride precipitates, which were uniformly distributed in the In939 matrix. These precipitates suppressed grain growth during solidification, resulting in a refined microstructure and significant crack inhibition, as validated through X-ray CT analysis.

The In939+2TiB_2 composite exhibited a remarkable improvement in mechanical properties, achieving approximately 1.5 times the yield strength and ultimate tensile strength of pure In939, while maintaining favorable ductility (13–15 %). At elevated temperatures, the In939+5TiB_2 composite outperformed both In939+2TiB_2 and previously reported additively manufactured In939 alloys, demonstrating the beneficial effect of TiB_2 reinforcement in enhancing high-temperature mechanical performance.

The enhanced properties of TiB_2-reinforced composites arise from a combination of strengthening mechanisms, including grain boundary strengthening, solid solution strengthening, an increased dislocation density due to the coefficient of thermal expansion (CTE) mismatch, and compositional micro-segregation. These findings show the potential of TiB_2 as an effective reinforcing agent to overcome printability challenges and improve the mechanical performance of In939 alloys.

Overall, the scalability and robustness of the LPBF process for TiB_2-

doped composites demonstrate its promise for applications in extreme environments, such as aerospace and energy sectors. Future work should focus on optimizing the TiB_2 content, LPBF processing parameters, and post-processing strategies to achieve balanced mechanical performance at both room and elevated temperatures.

CRediT authorship contribution statement

Jong-Soo Bae: Writing – review & editing, Writing – original draft, Validation, Methodology, Investigation, Formal analysis, Data curation, Visualization. **Emre Tekoglu:** Writing – review & editing, Writing – original draft, Visualization, Validation, Methodology, Investigation, Formal analysis, Data curation, Conceptualization. **Mohammed Alrizqi:** Writing – original draft, Formal analysis, Data curation. **Alexander D. O'Brien:** Writing – review & editing, Data curation. **Jian Liu:** Data curation. **Krista Biggs:** Data curation. **So Yeon Kim:** Data curation. **Aubrey Penn:** Data curation. **Ivo Sulak:** Data curation. **Wen Chen:** Writing – review & editing, Visualization, Validation, Supervision. **Kang Pyo So:** Writing – review & editing, Validation, Supervision. **A. John Hart:** Writing – review & editing, Validation, Supervision. **Gi-Dong Sim:** Writing – review & editing, Visualization, Validation, Supervision, Resources, Project administration, Funding acquisition, Data curation, Conceptualization. **Ju Li:** Writing – review & editing, Visualization, Validation, Supervision, Resources, Project administration, Methodology, Investigation, Funding acquisition, Data curation, Conceptualization.

Data availability

The data that support the findings of this study are available from the corresponding author upon reasonable request.

Declaration of competing interest

The authors declare that they have no known competing financial interests or personal relationships that could have appeared to influence the work reported in this paper.

Acknowledgment

This work was supported by Eni S.p.A. through the MIT Energy Initiative and by the Advanced Research Projects Agency-Energy (ARPA-E, Award #DE-AR0001434). GDS also acknowledges support by the National Research Foundation of Korea (NRF) (No. RS-2025-00520263 and 2023M2D2A1A01078149). 3D printing for this project was completed using the EOS M290 at the Advanced Digital Design and Fabrication core facility at the University of Massachusetts, Amherst. TEM studies were performed at MIT. nano's facilities and KAIST Analysis Center for Research Advancement (KARA). Lastly, the authors would like to thank Dr. James C. Weaver who helped carry out the micro-CT through the use of MIT.nano's facilities. The authors also would like to thank Prof. Greg Olson for his valuable assistance during Thermo-Calc studies.

Appendix A. Supplementary data

Supplementary data to this article can be found online at https://doi.org/10.1016/j.msea.2025.148446.

Data availability

Data will be made available on request.

References

[1] E. Nandha Kumar, K.S. Athira, S. Chatterjee, D. Srinivasan, Effect of Heat Treatment on Structure and Properties of Laser Powder Bed Fusion Inconel, 939, 2023, https://doi.org/10.1115/IAM2022-93945.
[2] T. Zou, M. Liu, Y. Cai, Q. Wang, Y. Jiang, Y. Wang, Z. Gao, Y. Pei, H. Zhang, Y. Liu, Q. Wang, Effect of temperature on tensile behavior, fracture morphology, and deformation mechanisms of Nickel-based additive manufacturing 939 superalloy, J. Alloys Compd. 959 (2023) 170559, https://doi.org/10.1016/J.JALLCOM.2023.170559.
[3] A.S. Shaikh, M. Rashidi, K. Minet-Lallemand, E. Hryha, On as-built microstructure and necessity of solution treatment in additively manufactured Inconel 939, Powder Metall. 939 (2022) 3–11, https://doi.org/10.1080/00325899.2022.2041787.
[4] B. Zhang, H. Ding, A.C. Meng, S. Nemati, S. Guo, W.J. Meng, Crack reduction in Inconel 939 with Si addition processed by laser powder bed fusion additive manufacturing, Addit. Manuf. 72 (2023) 103623, https://doi.org/10.1016/J.ADDMA.2023.103623.
[5] I. Šulák, T. Babinský, A. Chlupová, A. Milovanović, L. Náhlík, Effect of building direction and heat treatment on mechanical properties of Inconel 939 prepared by additive manufacturing, J. Mech. Sci. Technol. 37 (2023), https://doi.org/10.1007/s12206-022-2101-7.
[6] G. Marchese, S. Parizia, A. Saboori, D. Manfredi, M. Lombardi, P. Fino, D. Ugues, S. Biamino, The influence of the process parameters on the densification and microstructure development of laser powder bed fused inconel 939, Metals 10 (2020) 882, https://doi.org/10.3390/MET10070882, 2020, Vol. 10, Page 882.
[7] O.C. Ozaner, Ş. Karabulut, M. İzciler, Study of the surface integrity and mechanical properties of turbine blade fir trees manufactured in Inconel 939 using laser powder bed fusion, J. Manuf. Process. 79 (2022) 47–59, https://doi.org/10.1016/J.JMAPRO.2022.04.054.
[8] P. Kanagarajah, F. Brenne, T. Niendorf, H.J. Maier, Inconel 939 processed by selective laser melting: effect of microstructure and temperature on the mechanical properties under static and cyclic loading, Mater. Sci. Eng., A 588 (2013) 188–195, https://doi.org/10.1016/J.MSEA.2013.09.025.
[9] C. Zeng, H. Ding, U. Bhandari, S.M. Guo, Design of Crack-free Laser Additive Manufactured Inconel 939 Alloy Driven by Computational Thermodynamics Method, 12, 2022, pp. 844–849, https://doi.org/10.1557/s43579-022-00253-x.
[10] J. Raute, T. Jokisch, M. Biegler, M. Rethmeier, Effects on crack formation of additive manufactured Inconel 939 sheets during electron beam welding, Vacuum 195 (2022) 110649, https://doi.org/10.1016/J.VACUUM.2021.110649.
[11] S. Li, S. Gao, W. Zhang, G. Lu, L. Cui, L. Li, Y. Ma, S. Wang, Study of the crack and porosity regulation of a non-weldable Ni-Based superalloy fabricated by laser powder bed fusion, J. Mater. Eng. Perform. (2024) 1–12, https://doi.org/10.1007/S11665-024-10362-4/FIGURES/15.
[12] D.E. Cooper, N. Blundell, S. Maggs, G.J. Gibbons, Additive layer manufacture of Inconel 625 metal matrix composites, reinforcement material evaluation, J. Mater. Process. Technol. 213 (2013) 2191–2200, https://doi.org/10.1016/J.JMATPROTEC.2013.06.021.
[13] B. Zhang, G. Bi, P. Wang, J. Bai, Y. Chew, M.S. Nai, Microstructure and mechanical properties of Inconel 625/nano-TiB2 composite fabricated by LAAM, Mater. Des. (2016), https://doi.org/10.1016/j.matdes.2016.08.078.
[14] B. Zhang, G. Bi, S. Nai, C.N. Sun, J. Wei, Microhardness and microstructure evolution of TiB2 reinforced Inconel 625/TiB2 composite produced by selective laser melting, Opt Laser. Technol. (2016), https://doi.org/10.1016/j.optlastec.2016.01.010.
[15] M.Y. Shen, X.J. Tian, D. Liu, H.B. Tang, X. Cheng, Microstructure and fracture behavior of TiC particles reinforced Inconel 625 composites prepared by laser additive manufacturing, J. Alloys Compd. (2018), https://doi.org/10.1016/j.jallcom.2017.10.280.
[16] S.H. Kim, G.H. Shin, B.K. Kim, K.T. Kim, D.Y. Yang, C. Aranas, J.P. Choi, J.H. Yu, Thermo-mechanical improvement of Inconel 718 using ex situ boron nitride-reinforced composites processed by laser powder bed fusion, Sci. Rep. (2017), https://doi.org/10.1038/s41598-017-14713-1.
[17] E. Tekoğlu, A.D. O'Brien, J. Liu, B. Wang, S. Kavak, Y. Zhang, S.Y. Kim, S. Wang, D. Ağaoğulları, W. Chen, A.J. Hart, J. Li, Strengthening additively manufactured Inconel 718 through in-situ formation of nanocarbides and silicides, Addit. Manuf. 67 (2023) 103478, https://doi.org/10.1016/J.ADDMA.2023.103478.
[18] W.G. Fahrenholtz, G.E. Hilmas, Ultra-high temperature ceramics: materials for extreme environments, Scr. Mater. (2017), https://doi.org/10.1016/j.scriptamat.2016.10.018.
[19] E. Wuchina, E. Opila, M. Opeka, W. Fahrenholtz, I. Talmy, UHTCs: Ultra-High temperature ceramic materials for extreme environment applications, in: Electrochemical Society Interface, 2007, https://doi.org/10.1149/2.f04074if.
[20] Y. Zheng, F. Liu, W. Zhang, F. Liu, C. Huang, J. Gao, Q. Li, The microstructure evolution and precipitation behavior of TiB2/Inconel 718 composites manufactured by selective laser melting, J. Manuf. Process. 79 (2022) 510–519, https://doi.org/10.1016/J.JMAPRO.2022.04.070.
[21] Z. Zhang, Q. Han, S. Yang, Y. Yin, J. Gao, R. Setchi, Laser powder bed fusion of advanced submicrometer TiB2 reinforced high-performance Ni-based composite, Mater. Sci. Eng. 817 (2021) 141416, https://doi.org/10.1016/j.msea.2021.141416.
[22] Z. Zhang, Q. Han, Z. Liu, J. Gao, L. Wang, H. Liu, R. Wang, T. Ma, Z. Gao, Combined effects of heat treatment and TiB2 content on the high-temperature tensile performance of TiB2-modified Ni-based GH3230 alloy processed by laser powder bed fusion, Mater. Sci. Eng., A 861 (2022) 144379, https://doi.org/10.1016/J.MSEA.2022.144379.

[23] Z. Zhang, Q. Han, Z. Liu, L. Wang, H. Zhang, P. Zhao, G. Zhu, C. Huang, R. Setchi, Cracking behaviour and its suppression mechanisms with TiB2 additions in the laser additive manufacturing of solid-solution-strengthened Ni-based alloys, Compos. B Eng. 266 (2023) 111023, https://doi.org/10.1016/J.COMPOSITESB.2023.111023.
[24] Z. Zhang, Q. Han, Z. Liu, X. Wang, L. Wang, X. Yang, T. Ma, Z. Gao, Influence of the TiB2 content on the processability, microstructure and high-temperature tensile performance of a Ni-based superalloy by laser powder bed fusion, J. Alloys Compd. 908 (2022) 164656, https://doi.org/10.1016/J.JALLCOM.2022.164656.
[25] E. Tekoglu, J.-S. Bae, H.-A. Kim, K.-H. Lim, J. Liu, T.D. Doležal, S.Y. Kim, M. A. Alrizqi, A. Penn, W. Chen, A.J. Hart, J.-H. Kang, C.-S. Oh, J. Park, F. Sun, S. Kim, G.-D. Sim, J. Li, Superior high-temperature mechanical properties and microstructural features of LPBF-printed In625-based metal matrix composites, Mater. Today 80 (2024) 297–307, https://doi.org/10.1016/j.mattod.2024.09.006.
[26] X. Zhang, H. Chen, L. Xu, J. Xu, X. Ren, X. Chen, Cracking mechanism and susceptibility of laser melting deposited Inconel 738 superalloy, Mater. Des. 183 (2019) 108105, https://doi.org/10.1016/J.MATDES.2019.108105.
[27] P. Kontis, E. Chauvet, Z. Peng, J. He, A.K. da Silva, D. Raabe, C. Tassin, J. J. Blandin, S. Abed, R. Dendievel, B. Gault, G. Martin, Atomic-scale grain boundary engineering to overcome hot-cracking in additively-manufactured superalloys, Acta Mater. 177 (2019) 209–221, https://doi.org/10.1016/J.ACTAMAT.2019.07.041.
[28] C. Qiu, H. Chen, Q. Liu, S. Yue, H. Wang, On the solidification behaviour and cracking origin of a nickel-based superalloy during selective laser melting, Mater. Char. 148 (2019) 330–344, https://doi.org/10.1016/J.MATCHAR.2018.12.032.
[29] Y.T. Tang, C. Panwisawas, J.N. Ghoussoub, Y. Gong, J.W.G. Clark, A.A.N. Németh, D.G. McCartney, R.C. Reed, Alloys-by-design: application to new superalloys for additive manufacturing, Acta Mater. 202 (2021) 417–436, https://doi.org/10.1016/J.ACTAMAT.2020.09.023.
[30] J. Xu, Y. Ding, Y. Gao, H. Wang, Y. Hu, D. Zhang, Grain refinement and crack inhibition of hard-to-weld Inconel 738 alloy by altering the scanning strategy during selective laser melting, Mater. Des. 209 (2021) 109940, https://doi.org/10.1016/J.MATDES.2021.109940.
[31] Y.L. Hu, X. Lin, X.B. Yu, J.J. Xu, M. Lei, W.D. Huang, Effect of Ti addition on cracking and microhardness of Inconel 625 during the laser solid forming processing, J. Alloys Compd. 711 (2017) 267–277, https://doi.org/10.1016/J.JALLCOM.2017.03.355.
[32] Z. Yu, C. Guo, S. Han, X. Hu, L. Cao, Z. Xu, H. Ding, Q. Zhu, The effect of Hf on solidification cracking inhibition of IN738LC processed by selective laser melting, Mater. Sci. Eng., A 804 (2021) 140733, https://doi.org/10.1016/J.MSEA.2021.140733.
[33] Y.L. Wang, L. Zhao, D. Wan, S. Guan, K.C. Chan, Additive manufacturing of TiB2-containing CoCrFeMnNi high-entropy alloy matrix composites with high density and enhanced mechanical properties, Mater. Sci. Eng., A 825 (2021) 141871, https://doi.org/10.1016/j.msea.2021.141871.
[34] X. Xie, Y. Ma, C. Chen, G. Ji, C. Verdy, H. Wu, Z. Chen, S. Yuan, B. Normand, S. Yin, H. Liao, Cold spray additive manufacturing of metal matrix composites (MMCs) using a novel nano-TiB2-reinforced 7075Al powder, J. Alloys Compd. 819 (2020) 152962, https://doi.org/10.1016/j.jallcom.2019.152962.
[35] Q.Z. Wang, X. Lin, N. Kang, X.L. Wen, Y. Cao, J.L. Lu, D.J. Peng, J. Bai, Y.X. Zhou, M. El Mansori, W.D. Huang, Effect of laser additive manufacturing on the microstructure and mechanical properties of TiB2 reinforced Al-Cu matrix composite, Mater. Sci. Eng., A 840 (2022) 142950, https://doi.org/10.1016/j.msea.2022.142950.
[36] M.J. Aziz, T. Kaplan, Continuous growth model for interface motion during alloy solidification, Acta Metall. 36 (1988) 2335–2347, https://doi.org/10.1016/0001-6160(88)90333-1.
[37] T.W. Clyne, M. Wolf, W. Kurz, The effect of melt composition on solidification cracking of steel, with particular reference to continuous casting, Metall. Trans. A B 13 (1982) 259–266, https://doi.org/10.1007/BF02664583/METRICS.
[38] Suyitno, W.H. Kool, L. Katgerman, Hot tearing criteria evaluation for direct-chill casting of an Al-4.5 pct Cu alloy, Metall. Mater. Trans. A Phys. Metall. Mater. Sci. 36 (2005) 1537–1546, https://doi.org/10.1007/S11661-005-0245-6/METRICS.
[39] Y. Tian, A. Gontcharov, R. Gauvin, P. Lowden, M. Brochu, Effect of heat treatment on microstructure evolution and mechanical properties of Inconel 625 with 0.4wt % boron modification fabricated by gas tungsten arc deposition, Mater. Sci. Eng., A 684 (2017) 275–283, https://doi.org/10.1016/j.msea.2016.12.038.
[40] S. Kou, Solidification and liquation cracking issues in welding, J. Occup. Med. 55 (2003) 37–42, https://doi.org/10.1007/s11837-003-0137-4.
[41] I. Rodríguez-Barber, A.M. Fernández-Blanco, I. Unanue-Arruti, I. Madariaga-Rodríguez, S. Milenkovic, M.T. Pérez-Prado, Laser powder bed fusion of the Ni superalloy Inconel 939 using pulsed wave emission, Mater. Sci. Eng., A 870 (2023) 144864, https://doi.org/10.1016/J.MSEA.2023.144864.
[42] E. Tekoğlu, A.D. O'Brien, J.-S. Bae, K.-H. Lim, J. Liu, S. Kavak, Y. Zhang, S.Y. Kim, D. Ağaoğulları, W. Chen, A.J. Hart, G.-D. Sim, J. Li, Metal matrix composite with superior ductility at 800 °C: 3D printed In718+ZrB2 by laser powder bed fusion, Compos. B Eng. (2023) 111052, https://doi.org/10.1016/J.COMPOSITESB.2023.111052.
[43] X. Yao, S.K. Moon, B.Y. Lee, G. Bi, Effects of heat treatment on microstructures and tensile properties of IN718/TiC nanocomposite fabricated by selective laser melting, Int. J. Precis. Eng. Manuf. 18 (2017) 1693–1701, https://doi.org/10.1007/s12541-017-0197-y.
[44] Q. song Song, Y. Zhang, Y. feng Wei, X. yi Zhou, Y. fu Shen, Y. min Zhou, X. mei Feng, Microstructure and mechanical performance of ODS superalloys manufactured by selective laser melting, Opt Laser. Technol. 144 (2021) 107423, https://doi.org/10.1016/J.OPTLASTEC.2021.107423.
[45] M.M. Kirka, F. Medina, R. Dehoff, A. Okello, Mechanical behavior of post-processed Inconel 718 manufactured through the electron beam melting process, Mater. Sci. Eng., A 680 (2017) 338–346, https://doi.org/10.1016/J.MSEA.2016.10.069.
[46] D. Zhang, W. Niu, X. Cao, Z. Liu, Effect of standard heat treatment on the microstructure and mechanical properties of selective laser melting manufactured Inconel 718 superalloy, Mater. Sci. Eng., A 644 (2015) 32–40, https://doi.org/10.1016/J.MSEA.2015.06.021.
[47] H. Qi, M. Azer, A. Ritter, Studies of standard heat treatment effects on microstructure and mechanical properties of laser net shape manufactured INCONEL 718, n.d. https://doi.org/10.1007/s11661-009-9949-3, 2009.
[48] M. Mohsin Raza, Y.-L. Lo, Experimental investigation into microstructure, mechanical properties, and cracking mechanism of IN713LC processed by laser powder bed fusion, Mater. Sci. Eng., A 819 (2021) 141527, https://doi.org/10.1016/j.msea.2021.141527.
[49] A. Jena, S.E. Atabay, M. Brochu, Microstructure and mechanical properties of crack-free Inconel 738 fabricated by laser powder bed fusion, Mater. Sci. Eng., A 850 (2022) 143524, https://doi.org/10.1016/j.msea.2022.143524.
[50] G. Meng, Y. Gong, J. Zhang, Q. Ren, J. Zhao, Microstructure effect on the machinability behavior of additive and conventionally manufactured Inconel 718 alloys, J. Mater. Process. Technol. 324 (2024) 118228, https://doi.org/10.1016/J.JMATPROTEC.2023.118228.
[51] S. Griffiths, H. Ghasemi Tabasi, T. Ivas, X. Maeder, A. De Luca, K. Zweiacker, R. Wróbel, J. Jhabvala, R.E. Logé, C. Leinenbach, Combining alloy and process modification for micro-crack mitigation in an additively manufactured Ni-base superalloy, Addit. Manuf. 36 (2020) 101443, https://doi.org/10.1016/J.ADDMA.2020.101443.
[52] J.H. Martin, B.D. Yahata, J.M. Hundley, J.A. Mayer, T.A. Schaedler, T.M. Pollock, 3D printing of high-strength aluminium alloys, Nature 549 (2017) 365–369, https://doi.org/10.1038/nature23894, 2017 549:7672.
[53] I.S. Lee, C.J. Hsu, C.F. Chen, N.J. Ho, P.W. Kao, Particle-reinforced aluminum matrix composites produced from powder mixtures via friction stir processing, Compos. Sci. Technol. 71 (2011) 693–698, https://doi.org/10.1016/j.compscitech.2011.01.013.
[54] Q. Zhang, B.L. Xiao, W.G. Wang, Z.Y. Ma, Reactive mechanism and mechanical properties of in situ composites fabricated from an Al–TiO2 system by friction stir processing, Acta Mater. 60 (2012) 7090–7103, https://doi.org/10.1016/j.actamat.2012.09.016.
[55] H. Kou, W. Li, J. Ma, J. Shao, Y. Tao, X. Zhang, P. Geng, Y. Deng, Y. Li, X. Zhang, F. Peng, Theoretical prediction of the temperature-dependent yield strength of solid solution strengthening nickel-based alloys, Int. J. Mech. Sci. 140 (2018) 83–92, https://doi.org/10.1016/j.ijmecsci.2018.02.042.
[56] E.I. Galindo-Nava, L.D. Connor, C.M.F. Rae, On the prediction of the yield stress of unimodal and multimodal γ′ nickel-base superalloys, Acta Mater. 98 (2015) 377–390, https://doi.org/10.1016/j.actamat.2015.07.048.
[57] R. Labusch, A statistical theory of solid solution hardening, Phys. Status Solidi 41 (1970) 659–669, https://doi.org/10.1002/pssb.19700410221.
[58] L.A. Gypen, A. Deruyttere, Multi-component solid solution hardening, J. Mater. Sci. 12 (1977) 1028–1033. https://api.semanticscholar.org/CorpusID:135720775.
[59] P.A. Maksimiyuk, V.A. Gley, M. Hamerský, P. Lukáč, Z. Trojanová, Temperature dependence of Young's modulus of α-zirconium polycrystals, Phys. Status Solidi 107 (1988) K11–K13, https://doi.org/10.1002/pssa.2211070149.
[60] V.S. Erasov, E.N. Pirogov, V.P. Konoplenko, V.A. Akimkin, A.P. Marukhin, A. M. Tsirlin, E.A. Shchetilina, N.M. Balagurova, Temperature dependence of mechanical properties of boron fibers, Mech. Compos. Mater. 18 (1982) 127–130, https://doi.org/10.1007/BF00604829.
[61] W. Li, J. Ma, H. Kou, J. Shao, X. Zhang, Y. Deng, Y. Tao, D. Fang, Modeling the effect of temperature on the yield strength of precipitation strengthening Ni-base superalloys, Int. J. Plast. 116 (2019) 143–158, https://doi.org/10.1016/j.ijplas.2019.01.002.
[62] W.Z. Zou, X. Guo, X. Xie, X. Wang, Titanium handbook, Chem. Ind. Press 2 (2012) 8–9.
[63] K.W. Katahara, M. Nimalendran, M.H. Manghnani, E.S. Fisher, Elastic moduli of paramagnetic chromium and Ti-V-Cr alloys, J. Phys. F Met. Phys. 9 (1979) 2167, https://doi.org/10.1088/0305-4608/9/11/008.
[64] P.E. Armstrong, H.L. Brown, Anomalous temperature dependence of elastic moduli of niobium metal, Am. Soc. Metals, Trans. Quart. 58 (1965).
[65] G. V Zakharova, I.A. Popov, L.P. Zhorova, B. V Fedin, Niobium and its Alloys, Metallurgizdat, Moscow, 1961, p. 213.
[66] W. Köster, Die Temperaturabhängigkeit des blastizitätsmoduls reiner Metalle, Int. J. Mater. Res. 39 (1948) 1–9.
[67] J.W. Cahn, Hardening by spinodal decomposition, in: Symposium on the Role of Substructure in the Mechanical Behavior of Metals, Directorate of Materials and Processes, Aeronautical Systems Division, Air, 1963, p. 375.
[68] T.R. Smith, J.D. Sugar, C. San Marchi, J.M. Schoenung, Strengthening mechanisms in directed energy deposited austenitic stainless steel, Acta Mater. 164 (2019) 728–740, https://doi.org/10.1016/j.actamat.2018.11.021.
[69] G.P. Sabol, R. Stickler, Microstructure of nickel-based superalloys, Phys. Status Solidi 35 (1969) 11–52, https://doi.org/10.1002/pssb.19690350102.
[70] K. Lin, S.D. Pang, The influence of thermal residual stresses and thermal generated dislocation on the mechanical response of particulate-reinforced metal matrix nanocomposites, Compos. B Eng. 83 (2015) 105–116, https://doi.org/10.1016/j.compositesb.2015.08.008.
[71] S. Scudino, G. Liu, K.G. Prashanth, B. Bartusch, K.B. Surreddi, B.S. Murty, J. Eckert, Mechanical properties of Al-based metal matrix composites reinforced with Zr-

based glassy particles produced by powder metallurgy, Acta Mater. 57 (2009) 2029–2039, https://doi.org/10.1016/j.actamat.2009.01.010.
[72] M.L. Emiliani, Characterization and oxidation resistance of hot-pressed chromium diboride, Mater. Sci. Eng., A 172 (1993) 111–124, https://doi.org/10.1016/0921-5093(93)90431-D.
[73] EOS GmbH, EOS NickelAlloy IN939 Material Data Sheet Metal Solutions, 2022.
[74] W.S. Miller, F.J. Humphreys, Strengthening mechanisms in particulate metal matrix composites, Scripta Metall. Mater. 25 (1991) 33–38, https://doi.org/10.1016/0956-716X(91)90349-6.
[75] W. Mottay, P. Maugis, M. Jouiad, F. Roch, C. Perrin-Pellegrino, K. Hoummada, Effect of dislocation density on competitive segregation of solute atoms to dislocations, Mater. Sci. Eng., A 881 (2023) 145380, https://doi.org/10.1016/j.msea.2023.145380.